MICHIGAN STATE UNIVERSITY

CYCLOTRON LABORATORY

SPACE-TIME EVOLUTION OF THE REACTIONS ^{14}N + ^{27}Al, ^{197}Au AT E/A = 75 MeV AND ^{129}Xe + ^{27}Al, ^{122}Sn AT E/A = 31 MeV PROBED BY TWO-PROTON INTENSITY INTERFEROMETRY

W.G. GONG, C.K. GELBKE, W. BAUER, N. CARLIN,
R.T. de SOUZA, Y.D. KIM, W.G. LYNCH,
T. MURAKAMI, G. POGGI, D.P. SANDERSON,
M.B. TSANG, H.M. XU, D.E. FIELDS,
K. KWIATKOWSKI, R. PLANETA, V.E. VIOLA, Jr.,
S.J. YENNELLO, and S. PRATT

OCTOBER 1990

MSUCL-747

MSUCL-747
October, 1990

"Space-time evolution of the reactions $^{14}N+^{27}Al$, ^{197}Au at E/A=75 MeV and $^{129}Xe+^{27}Al$, ^{122}Sn at E/A=31 MeV probed by two-proton intensity interferometry"

W.G. Gong,, C.K. Gelbke, W. Bauer, N. Carlin,† R.T. de Sousa, Y.D. Kim, W.G. Lynch, T. Murakami,* G. Poggi,†† D.P. Sanderson, M.B. Tsang, and H.M. Xu
National Superconducting Cyclotron Laboratory
and Department of Physics and Astronomy,
Michigan State University, East Laming, MI 48824, USA

D.E. Fields, K. Kwiatkowski, R. Planeta,# V.E. Viola, Jr,., aud S.J. Yennello
Indiana University Cyclotron Facility,
Indiana University, Bloomington, IN 47405, USA

S. Pratt
Department of Physics, University of Wisconsin, Madison, WI 53706, USA

† Present address: Instituto de Física, Universidade de São Paulo, C. Postal 20516, CRP 01498, São Paulo, Brazil

* Present address: Department of Physics, Kyoto University, Kyoto 606, Japan

tt Permanent address: Dipartimento di Fisica dell' Università and INFN, Largo Enrico Fermi 2, 50125 Firenze, Italy

Present address: Institute of Nuclear Physics, Jagellonian University, Krakow, Poland

Abstract

Two-proton correlation functions have been measured at $\theta_{lab} \approx 25^\circ$ for the "forward kinematics" reactions $^{14}N+^{27}Al$, $^{14}N+^{197}Au$ at E/A=75 MeV, for the "inverse kinematics" reaction $^{129}Xe+^{27}Al$ at E/A=31 MeV, and for the nearly symmetric reaction $^{129}Xe+^{122}Sn$ at E/A=31 MeV. For the reactions at 76 MeV per nucleon, the correlation functions exhibit pronounced maxima at relative proton momenta, q≈20 MeV/c, and minima at q≈0 MeV/c. These correlations indicate emission from fast, nonequilibrium processes. They are analyeed in terms of standard Gaussian source parametrisations and compared to microscopic simulations performed with the Boltzmann-Uehling-Uhlenbeck equation. For the reactions at 31 MeV per nucleon, the two-proton correlation functions do not exhibit maxima at q≈20 MeV, but only minima at q≈0 MeV/c. These correlations indicate emission on a slower time scale. They can be reproduced by calculations based on the Weisskopf fomula for evaporative emission from fully equilibrated compound nuclei. For all reactions, the measured longitudinal and transverse correlation functions are very similar, in agreement with theoretical predictions.

PACS index: 25.70 Np

1. *Introduction*

Two protons, emitted at small relative momenta from an excited nuclear system, carry information about the space-time characteristics of the emitting source [1-20] since the relative two-proton wave function reflects the interplay of the mutual Coulomb and nuclear interactions and the Pauli exclusion principle [1,2,10,20]. The average distance between the two emitted protons depends on the spatial dimension and the lifetime of the emitting system. Consider two protons with an average velocity, v, emitted from a static source of radius, r, and lifetime, τ. After emission, the separation between the two protons is $r+v\tau$. For the decay of equilibrated compound nuclei with temperatures below 5 MeV, estimated emission times are larger than several hundred fm/c [21]. As a consequence, the average distance between emitted particles is much larger than the size of the emitting nucleus and the effects of the Coulomb interaction and the Pauli principle should dominate. On the other hand, nonequilibrium light particle emission in intermediate energy heavy ion collisions is calculated to proceed on much shorter time scales [22,23] and average particle separations may reflect the spatial dimension of the emitting system rather than the emission rate. Here, the nuclear interaction should be prominent.

Figure 1 illustrates the apparent sources expected for emission from short-lived and long-lived nuclear systems [24]. For correlations at small relative momenta, the detected particles have nearly the same final momenta directed towards the detection system. The dots in the figure illustrate the locations of protons, moving towards the detector with a given momentum, $\vec{p}$. Protons emitted from a short-lived source (upper part) occupy a small region of space, but protons emitted from a long-lived source (lower part) occupy a large and elongated region of space [10,12,24]. The direction of elongation is along the direction of $\vec{p}$. In general, reduced correlations are expected for emission from long-lived sources due to the larger apparent source size. Moreover, for an elongated source, the Pauli anti-correlation should be less in the longitudinal (elongated) direction than in the transverse (non-elongated) direction. The longitudinal correlation function (for which the relative momentum, $\vec{q}=\frac{1}{2}(\vec{p}_1-\vec{p}_2)$, is parallel to total momentum, $\vec{P}=\vec{p}_1+\vec{p}_2$) of a long-lived source may therefore be enhanced

as compared to the transverse correlation function (for which $\vec{q}$ is perpendicular to $\vec{P}$), unless the apparent source region becomes so large that sensitivity to antisymmetrization effects is lost.

In most measurements of two-proton correlation functions, implicit summations over the relative angle, $\Psi=\cos^{-1}(\vec{P}\cdot\vec{q}/Pq)$, between relative and total momenta of the proton pair were performed. While such measurements did not explore the shape of the source function, they did corroborate the qualitative expectations based upon the lifetime arguments outlined above. Two-proton correlation functions measured in kinematic regions dominated by evaporation from equilibrated reaction residues [13,16,17,18] exhibit a minimum at q≈0 MeV/c, but no maximum at q≈20 MeV/c. The shapes of these correlation functions could only be described by assuming emission from long-lived compound nuclei or, alternatively, from short-lived systems of unphysically large dimensions. In contrast, two-proton correlation functions measured in kinematic regions dominated by fast nonequilibrium emissions exhibit a clear maximum at q≈20 MeV/c [3-9,11,12,14,15,18,19] which becomes more pronounced with increasing kinetic energy of the emitted protons [4,6-9,12,18,19]. The shapes of these correlation functions could be described in terms of short-lived sources with dimensions comparable to those of the respective compound nuclei; emission from systems with even smaller dimensions was required for the description of correlation functions measured for the most energetic protons [4,7,9].

More recently, longitudinal and transverse correlation functions were measured, both for nonequilibrium [12] as well as equilibrium emissions [16,18]. None of these investigations found definitive evidence for elongated source shapes. For the case of equilibrium emission, these findings were shown to be consistent with theoretical correlation functions predicted by the Weisskopf formula for evaporation from equilibrated compound nuclei [16,18].

In order to elucidate similarities and differences of two-proton correlation functions for equilibrium and nonequilibrium emission processes, we performed measurements at $\theta_{lab}\approx 25^{\circ}$ for ^{14}N induced reactions on ^{27}Al and

^{197}Au at E/A=75 MeV and for ^{129}Xe induced reactions on ^{27}Al and ^{122}Sn at E/A=31 MeV. When light projectiles impinge on heavy target nuclei, emission at forward angles is dominated by nonequilibrium processes and emission at backward angles is dominated by equilibrium processes, see e.g. refs. [8,15,16]. Taking advantage of this angular dependence, we studied nonequilibrium emission in "forward kinematics" for the reactions ^{14}N+^{27}Al and ^{14}N+^{197}Au at E/A=75 MeV and equilibrium emission in "inverse kinematics" for the reaction ^{129}Xe+^{27}Al and for the nearly-symmetric reaction ^{129}Xe+^{122}Sn at E/A=31 MeV. The measurements were performed with identical detector geometries, energy calibrations and energy thresholds.

Experimental details are given in Section 2. In Section 3, the single-particle inclusive proton cross sections are shown. The measured two-proton correlation functions are presented in Section 4 and discussed in terms of short-lived Gaussian sources to allow comparisons with previous analyses. In Section 5, correlation functions for equilibrium emissions are compared to predictions of the Weisskopf evaporation model. In Section 6, correlation functions for nonequilibrium emissions are compared to predictions of the Boltzmann-Uehling-Uhlenbeck model. A summary and conclusions are given in Section 7. First results of this series of experiments have been published previously [18,19].

2. *Experimental Details*

The experiment was performed in the 92 inch scattering chamber of the National Superconducting Cyclotron Laboratory of Michigan State University using beams from the K1200 cyclotron. Typical beam intensities on target were approximately 5×10^{9} ^{14}N-ions per second at E/A=75 MeV and 1×10^{8} ^{129}Xe-ions per second at E/A=31 MeV. The beam spots on target had elongated shapes of typically 1-2 mm width and 2-3 mm height. For reactions induced by ^{129}Xe, we used ^{27}Al and ^{122}Sn targets with areal densities of 5.6 and 5.3 mg/cm^2, respectively. For reactions induced by ^{14}N, we used ^{27}Al and ^{197}Au targets with areal densities of 15.0 and 15.9 mg/cm^2, respectively.

Light particles were detected with two ΔE-E detector arrays consisting of silicon ΔE-detectors and CsI(Tl) or NaI(Tl) E-detectors. Figure 2 shows

the angles covered by individual telescopes in the the θ-ϕ plane, where θ and ϕ denote the polar and azimuthal angles with respect to the beam axis.

One array consisted of 37 Si-CsI(Tl) telescopes; it was centered at the polar and azimuthal angles of θ=25° and ϕ=0°. Each telescope of this array subtended a solid angle of $\Delta\Omega$=0.37 msr and consisted of a 300 μm thick planar surface barrier detector of 450 mm^2 active area and a cylindrical CsI(Tl) scintillator (length 10 cm, diameter 4 cm) read out by a 400 mm^2 PIN diode [25,26]. The nearest neighbor spacing between adjacent detectors was $\Delta\theta$=2.6°. The CsI(Tl) detector array was kept at a constant temperature and had excellent gain stability (better than 1% over a time period of one month).

The other array consisted of 13 Si-NaI(Tl) telescopes; it was centered at the polar and azimuthal angles of θ=25° and ϕ=90°. Each telescope of this array subtended a solid angle of $\Delta\Omega$=0.5 msr and consisted of a 400 μm thick surface barrier detector of 200 mm^2 active area and a cylindrical NaI(Tl) scintillator (length 10 cm, diameter 4 cm) read out by a photomultiplier tube. The nearest neighbor spacing between adjacent detectors was $\Delta\theta$=4.4°. Energy calibrations of individual detectors were obtained by scattering α-particles of 90, 116, and 160 MeV incident energy from a $(CH_2)_n$ target and detecting elastically scattered α-particles and recoil protons at various laboratory angles. Gain drifts of the individual photomultiplier tubes were measured by a light pulser system as well as by changes in the location of the particle identification lines in the ΔE-E matrix [8]. These gain drifts were determined in the off-line analysis and corrected with an overall accuracy of better than 2%.

Coincidence and downscaled singles data were taken simultaneously. Energy calibrations are accurate to better than 2%. Typical detector energy resolutions were of the order of 2% and 1% for protons of 40 MeV and 100 MeV, respectively. In our data analysis, a software energy threshold of 10 MeV was applied, and all coincidence data were corrected for random coincidences.

3. *Inclusive Energy Spectra*

Examples of inclusive energy spectra for protons detected at the extreme angles covered by our detector array, Θ_{lab} = 18° and 33°, are shown in Fig. 3. Spectra measured for reactions induced by ^{129}Xe and ^{14}N projectiles are shown in the left and right panels, respectively. In order to gain qualitative insight and allow comparisons with other data, we have fit these cross sections with simple analytic functions. We have to caution, however, that the extracted parameters are not uniquely determined by our data and must not be overinterpreted since our measurements covered only a small range of emission angles.

For the ^{14}N-induced reactions, we have chosen a simple three-source parametrization, representing isotropic Maxwellian contributions from a target-like source, a projectile-like source, and an intermediate velocity nonequilibrium source:

$$\frac{d^2\sigma}{d\Omega\, dE} = \sum_{i=1}^{3} N_i \sqrt{E-U_c}\cdot e^{-[E-U_c+E_i-2\sqrt{E_i(E-U_c)}\cdot\cos\theta]/T_i} \quad . \qquad (1)$$

Here, N_i and T_i are relative normalization and kinetic temperature parameters, respectively. The energy E_i is the kinetic energy of a particle co-moving with the i-th source, $E_i=\frac{1}{2}mc^2\beta_i^2$. The Coulomb energy, U_c, corrects for the Coulomb repulsion from heavy reaction residues assumed at rest in the laboratory rest frame.

The solid curves displayed in the right hand panels of Fig. 3 show fits obtained with this parametrization; the parameters are listed in Table 1. The spectra can be rather well described by assuming emission from target- and projectile-like sources with temperature parameters of about 4 to 6 MeV and by including a nonequilibrium component described, as before [7,8,28], in terms of an intermediate velocity source characterized by a high kinetic temperature parameter, T≈18-20 MeV. Particularly for the ^{14}N+^{197}Au reaction, the fits indicate significant evaporative contributions from a target-like source to the low-energy portion of the spectrum.

For the Xe-induced reactions, fusion-like and projectile-like residues have large velocities in the laboratory rest frame, and emission from these two sources is strongly forward focussed. In comparison, contributions from target-like residues are of minor importance at our detection angles. Furthermore, nonequilibrium emission may be expected to be small. Therefore, we adopted a two-source parametrization representing emission from projectile- and fusion-like sources. For these sources, the simple Coulomb correction adopted in Eq. (1) is inappropriate since the heavy reaction residues have large velocities with respect to the laboratory rest frame. Furthermore, the measurements include energies which lie below the projectile and compound nucleus Coulomb barriers. Hence, the sharp truncation of the energy spectra for sub-barrier energies is inappropriate. For these reasons, we adopted a parametrization similar to that used in ref. [27]:

$$\frac{d^2\sigma}{d\Omega\, dE} = \sum_{i=1}^{2} N_i \int_{U_l}^{U_u} dU \frac{\exp[-(U-U_c)^2/2\Delta_c^2]}{\Delta_c\sqrt{2\pi}} \sqrt{E(1-U/E_{cm,i})}\; e^{-(E_{cm,i}-U)/T_i} \quad . \quad (2)$$

Here, $E_{cm,i}=E+E_i-2\sqrt{E_i E}\cdot\cos\theta$ and $E_i=\frac{1}{2}mc^2\beta_i^2$; as in ref. [27], the integration limits were chosen as $U_l=\max(0,U_c-5\Delta_c)$ and $U_u=\min(E_{cm,i},U_c+5\Delta_c)$. In Eq. (2), the Coulomb field is assumed to be stationary in the rest frame of the emitting source, and an average is performed over an ensemble of Coulomb barriers using Gaussian weighting factors.

The fitted spectra are shown as solid lines in the left hand panels of Fig. 3. The spectra can be rather well described by assuming evaporative emission from a fusion-like source and a projectile-like source. (For the ^{129}Xe+^{27}Al reaction, fusion-like sources have velocities very similar to the projectile velocity, $\beta\approx 0.26$. For the ^{129}Xe+^{122}Sn reaction, fusion-like sources have approximately half the beam velocity.) The fits shown by the solid curves indicate strong contributions from decays of excited projectile residues. The inclusion of a projectile-like source largely improves the fits at lower energies. At these energies, the calculations are sensitive to details of the parametrization of the ensemble of Coulomb barriers. Again, it must be stressed that the extracted source parameters are not

uniquely determined because of the small angular range covered by our detector array. In order to illustrate some of the existing uncertainties, we have also described the tail of the energy spectra ($E \geq 40$ MeV) by assuming emission from a single source moving with the velocity of the compound nucleus. These calculations are shown by the dashed curves in the left hand panels of Fig. 3; the parameters are listed in Table 1.

It is not the purpose of the present investigation to provide a unique interpretation of the single-particle inclusive cross sections. The adopted parametrizations should, therefore, be viewed with a "grain of salt". Nevertheless, the calculations indicate possible contributions from a number of different sources which cannot be disentangled without ambiguity.

4. *Analysis with Spherical Sources of Negligible Lifetime*

The experimental two-particle correlation functions, R(q), are presented as a function of relative momentum, q, using the definition:

$$\Sigma Y_{12}(\vec{p}_1,\vec{p}_2) = C_{12}[1+R(q)]\Sigma Y_1(\vec{p}_1)Y_2(\vec{p}_2) \ . \qquad (3)$$

Here, $\vec{p}_1$ and $\vec{p}_2$ are the laboratory momenta of particles 1 and 2; $q=\frac{1}{2}|\vec{p}_1-\vec{p}_2|$ is the relative momentum of the particle pair; $Y_{12}(\vec{p}_1,\vec{p}_2)$ is the coincidence yield; and $Y_1(\vec{p}_1)$ and $Y_2(\vec{p}_2)$ are the single particle yields. For each experimental gating condition, the sums on both sides of Eq. (3) are extended over all energy and detector combinations corresponding to the given bins of q. The normalization constant, C_{12}, is determined by the requirement that R(q)=0 for large relative momenta.

Theoretical correlation functions are calculated with the formula [1,2,10,20]:

$$1+R(\vec{P},\vec{q}) = \int d^3r F_{\vec{P}}(\vec{r})|\Phi(\vec{q},\vec{r})|^2 \ . \qquad (4)$$

Here, $\vec{P}=\vec{p}_1+\vec{p}_2$ is the total momentum of the proton pair, $\Phi(\vec{q},\vec{r})$ is the relative two-proton wave function, and $F_{\vec{P}}(\vec{r})$ is defined by:

$$F_{\vec{P}}(\vec{r}) = \frac{\int d^3X f(\vec{P}/2,\vec{X}+\vec{r}/2,t_>) f(\vec{P}/2,\vec{X}-\vec{r}/2,t_>)}{|\int d^3X f(\vec{P}/2,\vec{X},t_>)|^2} \quad . \tag{5}$$

Here, the Wigner function, $f(\vec{p},\vec{r},t_>)$, is the phase-space distribution of particles of momentum $\vec{p}$ at position $\vec{r}$ at some time, $t_>$, after the emission process. The function $f(\vec{p},\vec{r},t_>)$ can be expressed in terms of the emission function, $g(\vec{p},\vec{r},t)$, i.e. the probability of emitting a particle with momentum $\vec{p}$ at location $\vec{r}$ and time t [20]:

$$f(\vec{p},\vec{r},t_>) = \int_{-\infty}^{t_>} dt\; g[\vec{p},\vec{r}-\vec{p}(t_>-t)/m,t] \quad . \tag{6}$$

In most previous analyses, $g(\vec{p},\vec{r},t)$ was parametrized in terms of a simple Gaussian source of negligible lifetime,

$$g(\vec{P}/2,\vec{r},t) = \rho_0 \delta(t) \exp[-r^2/r_0^2(P)] \quad . \tag{7}$$

To allow comparisons with these previous analyses and to systematize our data, we will adopt this parametrization for the calculations presented in this section. In Sects. 5 and 6 we will calculate correlation functions with more realistic distributions $f(\vec{p},\vec{r},t_>)$ calculated from the Weisskopf evaporation formula and from solutions of the semiclassical BUU transport equation, respectively.

4.1. Angle and energy integrated correlation functions

Two-proton correlation functions corresponding to sums over all detectors and all proton energies above the applied software energy threshold of 10 MeV are compared in Fig. 4. The correlation functions measured for the reactions $^{14}N+^{27}Al$ and $^{14}N+^{197}Au$ exhibit pronounced maxima at relative momenta $q \approx 20$ MeV, see top panels of Fig. 4. Small but significant differences exist at small relative momenta where the minimum at $q \approx 0$ is more pronounced for the ^{27}Al than for the ^{197}Au target. The correlation functions measured for the ^{129}Xe-induced reactions do not exhibit a pronounced maximum at $q \approx 20$ MeV, but only a minimum at $q \approx 0$ MeV/c, see bottom panels of Fig. 4. The correlation functions measured for the reactions $^{129}Xe+^{27}Al$ and

^{129}Xe+^{122}Sn have very similar shapes. On the other hand, the correlation functions measured for ^{14}N and ^{129}Xe induced reactions are strikingly different. For orientation, the solid lines show theoretical correlation functions predicted for Gaussian sources of negligible lifetime. For the reactions induced by ^{14}N and ^{129}Xe, radius parameters of r_0=4.4 and 70 fm were used, respectively. These source parameters should be compared to the equivalent radius parameters for Al and Au nuclei, r_0(Al)≈2.5 fm and r_0(Au)≈4.4 fm , which are obtained from tabulated [29] rms charge radii using the approximate relation $r_0=(2/3)^{1/2}r_{rms}$. For the ^{14}N-induced reactions a source radius of r_0=4.4 fm is not necessarily unreasonable. However, it is astonishing that this radius parameter exhibits no obvious dependence on the size of the target nucleus. A purely geometrical interpretation of the correlation function is, therefore, in doubt. For the large source parameter, r_0≈70 fm, used to describe the correlation functions measured for the ^{129}Xe induced reactions, a purely geometrical interpretation is clearly unphysical and the lifetime of the emitting system must play a major role.

4.2. Dependence on total momentum

Two-proton correlation functions are known to exhibit strong dependences on the energy of the emitted particles [4,6-9,12,18,19] or, equivalently, on the total momentum, $\vec{P}=\vec{p}_1+\vec{p}_2$, of the coincident proton pair. Figure 5 shows two-proton correlation functions for two representative momentum gates, measured for the reactions ^{129}Xe+^{27}Al (upper panel) and ^{129}Xe+^{122}Sn (lower panel). The momentum gates represented by the solid and open points correspond to protons emitted with kinetic energies below and above the compound nucleus Coulomb barriers, respectively. For the ^{129}Xe+^{27}Al reaction, the two momentum gates, P=480-570 and 660-750 MeV/c, select protons with kinetic energies of $E_{c.m.}$≈ 5-10 and 15-23 MeV, respectively, in the center-of-mass frame of reference (i.e. the rest frame of the compound nucleus). For the ^{129}Xe+^{122}Sn reaction, the two momentum gates, P=270-540 and 540-660 MeV/c, select protons with kinetic energies of $E_{c.m.}$≈ 1-15 and 15-27 MeV, respectively. As can be expected from qualitative time scale arguments, sub-barrier emission results in a reduction of the minimum at q≈0 MeV/c. Furthermore, correlation functions at sub-barrier

energies can suffer enhanced attenuations and/or distortions from sequential decays of primary fragments emitted in particle unbound states [21] and from deflections in the Coulomb field of the heavy reaction residue. Because of these additional complications, we will refrain from a more detailed analysis of two-proton correlation functions for protons emitted with sub-barrier energies. Calculations of two-proton correlation functions for evaporative processes will be presented in Section 5.

The correlation functions measured for the ^{14}N-induced reactions exhibit a more pronounced dependence on the total momentum of the detected proton pairs. Figures 6 and 7 show correlation functions for representative ranges of the total momentum, P, for the reactions $^{14}N+^{27}Al$ and $^{14}N+^{197}Au$, respectively. Consistent with previous measurements, the maximum at q≈20 MeV/c becomes more pronounced for larger total momenta, i.e. for the emission of more energetic particles. For the lowest momentum gate, P=270-390 MeV/c, the correlation functions are distinctly different for the two targets. For the ^{27}Al target, a clear maximum at q≈20 MeV/c is measured. For the ^{197}Au target, on the other hand, this maximum is barely visible and the shape of the correlation function resembles that measured for evaporative processes.

The solid curves in Figs. 6 and 7 show correlation functions calculated for Gaussian sources of negligible lifetime, Eq. (7), using momentum dependent source parameters shown in Fig. 8. In these calculations, appropriate averages over total momentum were performed, and the resolution of the hodoscope was taken into account. The overall trends of the data are well described. However, the shapes of the measured correlation functions are not reproduced in all details. The peaks of the calculated correlation functions are slightly narrower than the peaks of the measured correlation functions. The disagreement is particularly evident in the region around q≈30-40 MeV/c. In addition, for the $^{14}N+^{197}Au$ reaction, the adopted parametrization fails to reproduce the exact shape of the minimum at q≈0 MeV/c for the low momentum gate, P=270-390 MeV/c.

In order to provide a simple description of the momentum dependence of the two-proton correlation functions measured for the ^{14}N-induced reactions, we have constructed experimental correlation functions for a number of narrow gates placed on the total momentum, P. Each such correlation function was characterized in terms of a Gaussian source, Eq. (7), by requiring that the correlation function calculated for this source could reproduce the height of the maximum of the measured correlation function. The dependence of the extracted radius parameters on the total momentum of the detected particle pair, $r_0(P)$, is shown in Fig. 8. The error bars indicate estimated systematic errors. For the ^{14}N+^{197}Au reaction, the adopted parametrization fails to reproduce the shape of the minimum at q≈0 MeV/c for the low momentum gates, P<350 MeV/c. Here, the assumed monotonic dependence of the radius parameter on total momentum appears to be inadequate, and one may have to mix in additional contributions from much larger sources or, alternatively, from long lived evaporative processes to fit the shape of the minimum at q≈0 MeV/c. Because of the inherent ambiguities of such an approach, we did not pursue this possibility. Instead, we have indicated these possible contributions by open-ended error bars.

While the average correlation functions measured for the ^{14}N+^{27}Al and ^{14}N+^{197}Au reaction are very similar (see Fig. 4), significant differences surface when one explores the dependence on the total momentum of the proton pairs. Such more subtle differences, already apparent in the raw data shown in Figs. 6 and 7, are clearly revealed in Fig. 8. For the ^{14}N+^{197}Au reaction, the extracted source dimensions exhibit a nearly monotonic increase with decreasing total momentum of the detected proton pair. For the ^{14}N+^{27}Al reaction, on the other hand, the extracted source dimensions are rather constant over the range of P≈400-750 MeV/c. The extracted source dimensions are comparable for the two targets at high total momenta, $P \gtrsim 800$ MeV/c, indicating that very energetic particles are emitted by comparable processes. At low total momenta, $P \lesssim 500$ MeV/c, the extracted source dimensions are considerably larger for the reactions on ^{197}Au than for the reactions on ^{27}Al, most likely indicating larger contributions from slow evaporation processes for the ^{197}Au target.

4.3. Instrumental resolution

In order to evaluate instrumental distortions of the measured correlation functions, we have simulated the response of our experimental apparatus by taking its known energy and angular resolution into account. The solid curves in Fig. 9 show the undistorted correlation functions, calculated for Gaussian sources with the indicated radius parameters. The points are results of Monte Carlo calculations in which the angular and energy resolutions of the experimental apparatus are taken into account. In these calculations, the coincidence yield was taken as

$$Y_{12}(\vec{p}_1,\vec{p}_2) = [1+R(q)]Y_1(\vec{p}_1)Y_2(\vec{p}_2) \ , \qquad (8)$$

where the singles yields, $Y_1(\vec{p}_1)$ and $Y_1(\vec{p}_2)$, were taken from the single particle yields measured for the $^{14}N+^{27}Al$ reaction and R(q) was calculated by assuming a Gaussian source of negligible lifetime, Eq. (7), with the radius parameter given in the figure. Both singles and coincidence distributions were smeared by the energy and angular resolution of the experimental apparatus and sorted in the same way as the experimental data, using three representative momentum gates. The simulated correlation functions are in close agreement with the original, theoretically predicted correlation function. Except at very small relative momenta, line shape distortions caused by the resolution of the experimental apparatus are negligible. Note, in particular, the absence of visible distortions in the region of q≈30-40 MeV/c where the Gaussian-source fits deviate from the experimental correlation functions (see also Figs. 6 and 7).

5. *Evaporative Emission*

Correlation functions for particle evaporation from long-lived compound nuclei can be calculated by using the Wigner-function formalism [10,20], Eqs. (4-6). We have used the statistical model of ref. [21] to construct Wigner functions for evaporative emission from equilibrated compound nuclei. In this model, the average particle emission is calculated from the Weisskopf formula and cooling of the compound nucleus is calculated from the average mass and energy emission rates. Sub-barrier emission is not incorporated because of the use of the sharp cut-off approximation for the

inverse cross sections. For simplicity, the level density is approximated by that of an ideal Fermi gas at the density of normal nuclear matter.

5.1. Angle-integrated correlation functions

Since the inclusive cross sections are consistent with substantial contributions from evaporative emission from excited projectile residues, we calculate correlation functions for two extreme cases, (i) emission from a source at rest in the compound nucleus rest frame and (ii) emission from a source at rest in the projectile rest frame.

In Fig. 10, results of calculations assuming evaporation from compound nuclei are compared with two-proton correlation functions measured for the ^{129}Xe+^{27}Al and ^{129}Xe+^{122}Sn reactions. The curves represent calculations which were folded with the resolution of the experimental apparatus and averaged over the appropriate momentum bins using the experimental proton yields as relative weights. In order to illustrate the sensitivity of the calculated emission rates to the initial temperature of the emitting system, we used the compound nucleus values for the mass, A, and charge, Z, but treated the temperature as a free parameter. Good agreement between calculations and data is obtained for initial temperatures of about 7-10 MeV. For complete fusion of ^{129}Xe+^{27}Al and ^{129}Xe+^{122}Sn, initial temperatures of 8.2 and 10.3 MeV, respectively, are calculated if one assumes the level density of an ideal Fermi gas of normal nuclear matter density; the more common relation, $T^2=(8\ \text{MeV})\times E^*/A$, gives values of 5.8 and 7.3 MeV. However, the equilibrated emitting systems should have temperatures which are somewhat lower than those calculated for compound nuclei formed in complete fusion reactions [8,30-32] since some energy is carried away by nonequilibrium emission.

In Fig. 11 we compare the data with calculations for particle evaporation from equilibrated projectile residues assumed to move with the initial projectile velocity. For simplicity, we used the projectile values for the mass, A, and charge, Z, but treated the temperature as a free parameter. As before, the calculations were folded with the resolution of the experimental apparatus, and averaged over the appropriate momentum bins using the

experimental proton yields as relative weights. For projectile decays, the lower momentum bin, P=540-660 MeV/c, largely corresponds to subbarrier emission. Therefore, we only present calculations for the higher momentum bin, P=660-750 MeV/c. Reasonable agreement with the data is obtained for temperatures of about 10-15 MeV.

Fits to the correlation functions require higher temperatures when one assumes emission from projectile-like sources rather than emission from fusion-like sources. This is related to the fact that average emission times become shorter for increasing temperature and for increasing emission energy with respect to the rest frame of the decaying nucleus [20,21]. In our detection geometry and for our laboratory-momentum gates, the emitted particles have lower kinetic energies in the projectile rest frame than in the compound nucleus rest frame. For fixed temperature, the correlations are therefore attenuated if one assumes emission from the rest frame of the projectile as compared to emission from the rest frame of the compound nucleus. To reproduce the experimental correlation function, one must choose a higher temperature for the projectile-like source than for the fusion-like source.

Temperatures which provide the best description of the experimental correlation functions shown in Figs. 10 and 11 may be unrealistically high. However, it may also be unrealistic to assume pure equilibrium emission. Some emission should take place prior to equilibration. Such contributions would decrease the average lifetime of the emitting system and produce stronger correlations. Within the present equilibrium model, stronger correlations can be produced by raising the temperature of the source [20]. Clearly, some quantitative uncertainties about the exact nature of the emitting system remain. However, the qualitative interpretation of the measured two-proton correlation functions as predominantly caused by slow evaporative emission is not affected by our incomplete knowledge of the mass, temperature, and velocity of the decaying nucleus or by small contributions from nonequilibrium emission processes.

5.2. Longitudinal and transverse correlation functions

We have explored the dependence of the two-particle correlation function on the angle, $\Psi = \cos^{-1}(\vec{P}\cdot\vec{q}/Pq)$, between the relative and total momentum vectors of the proton pairs to search for clues on the source lifetime and shape [2,10,12,16]. As was illustrated in Fig. 1 and discussed in refs. [10,12,20,24], emission from a long-lived system produces phase-space distributions elongated in the longitudinal direction. Because of the reduced Pauli anti-correlation in this direction, the longitudinal correlation function ($\Psi \approx 0^\circ$ or 180°) of a long-lived source may be enhanced compared to the transverse correlation function ($\Psi \approx 90^\circ$), unless the average particle separations become so large that sensitivity to antisymmetrization effects is lost.

Figure 12 shows longitudinal and transverse two-proton correlation functions measured for the reactions ^{129}Xe+^{27}Al (top panel) and the ^{129}Xe+^{122}Sn (bottom panel). The longitudinal correlation functions, shown by solid points, were evaluated for the gate $|\cos\Psi_\ell| \geq 0.77$ (corresponding to the angular cuts of $\Psi_\ell = 0^\circ$-40° or 140°-180°). The transverse correlation functions, shown by open points, were evaluated for the gate $|\cos\Psi_t| \leq 0.5$ (corresponding to the angular cut of $\Psi_t = 60^\circ$-120°). For improved statistical accuracy, the gates on the total momenta of the proton pairs were made wider than in Fig. 10; the values are indicated in the figure. No statistically significant difference between longitudinal and transverse correlation functions is visible. However, this result does not contradict theoretical expectations for evaporation from long-lived compound nuclei. The solid and dotted curves in Fig. 12 show longitudinal and transverse correlation functions calculated for evaporative emission using the parameters indicated in the figure. The calculations were averaged over the appropriate momentum bins and folded with the resolution of the experimental apparatus. The predicted differences between transverse and longitudinal correlation functions are of the order of a few percent and, therefore, below the statistical sensitivity of the present experiment.

It was shown in ref. [20] that differences in the shapes of longitudinal and transverse correlation functions exhibit a strong dependence on the total momenta of the proton pairs. For emission from equilibrated

^{165}Ho compound nuclei, significant differences between longitudinal and transverse correlation functions are mainly predicted for large momenta, but not for small momenta corresponding to emission close to the barrier. Since evaporative cross sections decrease exponentially as a function of increasing kinetic energy of the emitted particles, integrals over wide momentum gates have predominant contributions from lower momenta for which the differences between longitudinal and transverse correlation functions are predicted to be small and difficult to detect. Unfortunately, the statistical accuracy of our experiment was insufficient for a more detailed exploration of longitudinal and transverse correlation functions at higher total momenta of the emitted proton pairs.

6. *Comparison with BUU calculations*

For intermediate energy nucleus-nucleus collisions, particle emission already sets in at the early, non-equilibrated stages of the reaction for which purely statistical treatments are clearly inappropriate. These early stages of the reaction can be treated in terms of semiclassical models based upon the Boltzmann-Uehling-Uhlenbeck equation [33,34] which describes the space-time evolution of the one-body phase-space distribution function. The theory incorporates mean-field effects, nucleon-nucleon collisions, and the Pauli-exclusion principle in the semiclassical approximation. Within the formalism of refs. [10,20], the knowledge of the one-body phase-space distribution function is sufficient for the characterization of the size and lifetime of the reaction zone formed in the nuclear collision and for the calculation of the two-proton correlation function at small relative momenta.

We solve the BUU equation by numerical methods which are similar to the ones introduced by ref. [33]. The major new numerical technique used in our present calculations is the treatment of the Pauli exclusion principle. By explicitly storing $\hat{f}(\vec{p},\vec{r},t)$ on a six-dimensional lattice in every time-step, we were able to greatly speed up the computer program without relaxing the accuracy of the treatment of the Pauli exclusion principle [35]. In our standard calculations, we used a stiff equation of state and energy-dependent free nucleon-nucleon cross sections. (For the present

reactions, the calculations exhibit little sensitivity to the stiffness of the equation of state [19,20].) The Wigner functions of emitted particles were constructed from nucleons emitted during a time interval of Δt_e=140 fm/c following initial contact of the colliding nuclei. Nucleons were considered as emitted when, during this time interval, the surrounding density fell below $\rho_e=\rho_0/8$ and when subsequent interaction with the mean field did not cause recapture into regions of higher density. This test for recapture was continued over a time interval of Δt=180 fm/c after contact. The finite size of our lattice did not allow us to explore much larger emission times. However, the consideration of much larger emission times would not necessarily lead to more reliable results since, in our present approximation, the nuclei are not stable over long time scales and the BUU calculations become inaccurate due to spurious decays. While our particular choice of the parameters Δt_e and ρ_e is reasonable, it involves a certain degree of arbitrariness. Typically, different reasonable choices of Δt_e and ρ_e modify the magnitude of the predicted correlation functions by 5-10%; in some instances, the sensitivity to these parameters can be larger [20]. For the reactions ^{14}N+^{27}Al and ^{14}N+^{197}Au, the correlation functions were calculated from the phase space points obtained from a total of 5250 and 4500 computational events, respectively, with impact parameters distributed according to their geometrical weights; appropriate averages over impact parameter, orientation of the reaction plane, and momenta of the outgoing particles were taken into account. More details of our calculations are given in refs. [20].

6.1. Singles cross sections

While it is our main purpose to test the space-time evolution of reactions predicted by the BUU theory, it may still be instructive to compare the single-particle cross sections measured for the ^{14}N-induced reactions with those predicted by BUU calculations. In Fig. 13, the solid points represent the measured single-proton cross sections for the reactions ^{14}N+^{27}Al (upper panel) and ^{14}N+^{197}Au (lower panel); cross sections predicted by BUU calculations are shown by open points. For the emission of energetic protons, the cross sections predicted by the BUU calculations are in rather good agreement with the data. However, at lower energies, $E \lesssim 70$ MeV, the

predicted cross sections are larger than the measured ones. At least part of this discrepancy may be attributed to the fact that the present calculations do not incorporate cluster emission. The formation and emission of clusters is expected to be particularly important when the phase space density is high, i.e. at low kinetic energies. In these regions of phase space, the flux of emitted nucleons will appear, in part, in the form of bound clusters. On the basis of these qualitative arguments, one can expect that proton cross sections predicted by BUU calculations should be larger than the experimental cross sections for free protons; the effect should be most pronounced for protons of low energies.

6.2. Angle integrated correlation functions

Two-proton correlation functions calculated from density distributions predicted by the BUU equation are compared, respectively, in Figs. 14 and 15 with our measurements for the $^{14}N+^{27}Al$ and $^{14}N+^{197}Au$ reactions at E/A=75 MeV. Shown are correlation functions with no selection on the angle, Ψ, between the total and relative momentum vectors of the proton pairs. The gates placed on the total laboratory momenta of the emitted proton pairs are indicated in the figures. Overall, two-proton correlation functions predicted by the BUU theory (solid curves) are in rather good agreement with the measured correlation functions (points). It is particularly gratifying that the calculations can qualitatively reproduce the observed strong dependence of the correlation functions on the total momentum of the emitted proton pairs. For the low-momentum gate of the $^{14}N+^{197}Au$ reaction, the maximum of the calculated correlation function is larger than that of the experimental correlation function, see Fig. 15. This discrepancy is not surprising since the emission of low-energy protons is expected to have significant contributions from slow evaporative processes which are not incorporated into our calculations. In fact, the existence of a strong evaporative component in the low-energy portion of the proton spectrum for the $^{14}N+^{197}Au$ reaction was already inferred from the shape of the minimum of the correlation function at $q \lesssim 15$ MeV/c (see Sect. 4.2) as well as from the shape of the single particle spectra (see Sect. 3). The inclusion of evaporative processes would lead to more extended Wigner functions and, hence, to more attenuated correlation functions.

For the $^{14}N+^{27}Al$ reaction, the sensitivity of the calculated correlation functions to the nuclear equation of state and the magnitude of the in-medium nucleon-nucleon cross section has already been discussed in refs. [19,20]. The calculations were shown to depend significantly on the magnitude of the in-medium cross sections, but only weakly on the stiffness of the equation of state. For illustration, Fig. 14 also shows calculations for which the in-medium cross sections were taken as one-half of the free nucleon-nucleon cross sections (dotted curves). For the low and intermediate momentum gates, the calculated correlation functions exhibit enhanced maxima when the in-medium cross sections are reduced. For the high momentum gate, this sensitivity is reduced. The agreement with the data is significantly worse for the calculations using the reduced in-medium cross sections. For the $^{14}N+^{197}Au$ reaction, dependences on the stiffness of the equation of state and the magnitude of the in-medium cross sections were not explored because calculations for this heavier target would have required large additional amounts of computer time.

A close comparison of Figs. 6 and 7 with Figs. 14 and 15 reveals that correlations functions calculated from the BUU theory provide an improved description of the shape of the experimental correlation functions in the region of q≈30-40 MeV/c as compared to those calculated for spherical Gaussian sources. This difference in line-shape is related to the fact that BUU calculations produce non-spherical phase-space distributions. For a more detailed discussion see ref. [20].

6.3. Longitudinal and transverse correlation functions

Figures 16 and 17 present longitudinal and transverse correlation functions measured for the $^{14}N+^{27}Al$ and $^{14}N+^{197}Au$ reactions at E/A=75 MeV, respectively. As before, longitudinal (solid points) and transverse (open points) correlation functions were evaluated for the gates $|\cos\Psi_l|\geq 0.77$ and $|\cos\Psi_t|\leq 0.5$, respectively. The upper and lower panels of the figures show data for different gates on the total momenta of the emitted particle pairs, P=270-420 MeV/c and P=420-780 MeV/c for the $^{14}N+^{27}Al$ reaction, and P=270-450 MeV/c and P=450-780 MeV/c for the $^{14}N+^{197}Au$ reaction. For each

gate, left and right hand panels show results obtained with different normalization conventions. The right hand panels depict longitudinal and transverse correlation functions normalized with a single normalization constant, C_{12}, which was determined, for each gate on P, by normalizing the angle integrated correlation function, $R_0(q)$, by the condition,

$$\int_{\Delta q} dq \cdot R_0(q) = 0 \ , \tag{9}$$

where Δq=60-100 MeV/c. With this normalization, longitudinal and transverse correlation functions gated by low total momenta (P=270-420 and 270-450 MeV/c, top right-hand panels of Figs. 16 and 17) attain distinctly different values for larger relative momenta, $q \gtrsim 40$ MeV/c. For higher total momenta (P=420-780 and 450-780 MeV/c, bottom right-hand panels of Figs. 16 and 17) differences at large relative momenta are less significant.

At small relative momenta, residual dynamical correlations are expected to be small and the use of a single normalization constant should be justified. With this presumption, we do not find statistically significant differences between longitudinal and transverse correlation functions at small relative momenta, $q \lesssim 30$ MeV/c. This experimental result is in agreement with that of ref. [12] for which the same (angle independent) normalization convention had been adopted.

We have checked by Monte-Carlo calculations that the different asymptotic values assumed by longitudinal and transverse correlation functions are not due to trivial effects of detector acceptance or resolution. These differences cannot be understood in terms of the present model for intensity interferometry. They might, however, be related to dynamical correlations caused by impact parameter averaging effects when the single particle distributions exhibit significant azimuthal asymmetries. We give a brief discussion of dynamical correlations caused by impact parameter averaging in the Appendix. However, we feel that the present BUU calculations may not model such effects to a sufficient degree of accuracy since the theory does not reproduce the low-energy portion of the energy spectrum

(see Fig. 13). One should, therefore, not expect to reproduce dynamical correlations at the required level of accuracy of a few percent.

The left hand panels in Figs. 16 and 17 show longitudinal and transverse correlation functions normalized independently over the relative-momentum interval, Δq=60-100 MeV/c, by separately enforcing the conditions,

$$\int_{\Delta q} dq \cdot R_{L,T}(q) = 0 \ , \qquad (10)$$

for the longitudinal and transverse correlation functions $R_L(q)$ and $R_T(q)$. With this renormalization, the longitudinal correlation functions gated by the low total momentum cuts (P=270-420 and 270-450 MeV/c, top left-hand panels of Figs. 16 and 17) exhibit larger maxima than the transverse correlation functions, qualitatively consistent with an elongated source or a source of finite lifetime. For the $^{14}N+^{27}Al$ reaction, this difference disappears for higher total momenta (P=420-780 MeV/c, bottom left-hand panel of Fig. 16). For the $^{14}N+^{197}Au$ reaction, the transverse correlation function for the higher momentum gate (P=450-780 MeV/c, bottom left-hand panel of Fig. 17) exhibits a larger maximum than the longitudinal correlation function, consistent with an oblate source.

We should caution, that independent normalizations of longitudinal and transverse correlation functions cannot be justified a priori. Therefore, the correlation functions shown in the left hand panels of Figs. 16 and 17 should not be misconstrued as experimental evidence for deformed source shapes. The different normalizations adopted for the construction of the correlation functions shown in the right and left hand panels of the two figures are only used to illustrate the uncertainties within which differences and similarities between longitudinal and transverse correlations are established experimentally.

Figure 18 shows theoretical predictions for longitudinal and transverse correlation functions for the $^{14}N+^{27}Al$ and $^{14}N+^{197}Au$ reactions. These calculations employed the same cuts on P and Ψ which were used in the data

analysis. Differences predicted for longitudinal and transverse correlation functions are small. They are of the order of the statistical uncertainty of our measurements, but considerably smaller than the systematic normalization uncertainties illustrated in Figs. 16 and 17. Without an accurate understanding of the distortions caused by dynamical correlations it appears futile to extract information on the shape of the phase space distributions of emitted particles from differences between longitudinal and transverse correlation functions.

7. Summary and conclusions

In summary, we have measured two-proton correlation functions for emission processes governed by different emission time scales. Fast nonequilibrium processes were investigated, in "forward kinematics", for ^{14}N-induced reactions on ^{27}Al and ^{197}Au at E/A=75 MeV. Slow evaporative processes were studied at E/A=31 MeV for the near-symmetric reaction ^{129}Xe+^{122}Sn and for the "inverse kinematics" reaction ^{129}Xe+^{27}Al. Two-proton correlation functions measured for these qualitatively different reaction mechanisms exhibit significant differences in shape. These differences are well understood in terms of the Wigner function formalism for two-proton intensity interferometry [2,10,20] once realistic reaction models are used to generate the one-body phase-space density distribution of the emitted protons.

Correlation functions measured for nonequilibrium emission in ^{14}N-induced reaction at E/A=75 MeV exhibit pronounced maxima at relative momenta q≈20 MeV/c and minima at q≈0 MeV/c. The maximum at q≈20 MeV/c is caused by the attractive singlet S-wave interaction between the two emitted protons. The minimum at q≈0 MeV/c reflects the combined effects of the Coulomb repulsion and the Pauli-exclusion principle. For these reactions, the emission time scales are sufficiently short that the final phase-space distributions of the emitted particles are of nuclear or smaller dimensions. The measured correlation functions can be rather well understood by applying the final-state-interaction-model of refs. [2,10,20] to one-body phase-space distributions predicted by the Boltzmann-Uehling-Uhlenbeck

transport equation. Correlation functions calculated for the $^{14}N+^{27}Al$ reaction exhibit significant sensitivity to the magnitude of the in-medium cross section, but only weak sensitivity to the stiffness of the equation of state. It is particularly gratifying that the theory can reproduce the observed strong dependence of the experimental correlation functions on the total momentum of the coincident proton pairs.

Correlation functions measured for evaporative processes in ^{129}Xe-induced reactions at E/A=31 MeV do not exhibit maxima at q≈20 MeV/c, but only minima at q≈0 MeV/c. For these reactions, rather small emission rates lead to large spatial separations between emitted particles and a loss of memory of the size of the emitting nucleus. The measured correlation functions can be rather well understood by applying the final-state-interaction-model of refs. [2,10,20] to one-body phase-space distributions predicted by statistical model calculations based on the Weisskopf formula. The predicted correlation functions exhibit only moderate sensitivity to detailed properties of the decaying nucleus.

For all cases investigated in this experiment, longitudinal and transverse correlation functions were found to be very similar. Our data could not provide definitive evidence for elongated source shapes expected from simple lifetime arguments. The experimental observations are, however, consistent with more detailed calculations for which the predicted differences between longitudinal and transverse correlation functions were too small to be detected by the present experiment.

This work is based upon work supported by the National Science Foundation under Grant numbers PHY-86-11210, PHY-89-13813, PHY-89-06116 and the Department of Energy under grant number DE.FG602-88ER.40404.A000. WGL acknowledges the receipt of U.S. Presidential Young Investigator Award and NC acknowledges partial support by the FAPESP, Brazil.

Appendix: Impact parameter averaging

Correlations between coincident particles do not only arise from quantum statistics and/or final state interactions, but also from a number of dynamical and kinematical effects. At large relative momenta, for example, the measured correlations can be strongly influenced by phase space restrictions imposed on finite systems by conservation laws [4,36-41], or by implicit averages over impact parameter and orientation of the reaction plane [38-43]. For example, the detection of a single particle will shift the total momentum of all remaining particles; for small systems this effect can lead to significant correlations at large relative momenta [4,36-41]. If the single-particle distribution is azimuthally anisotropic, the detection of one particle can filter out a non-isotropic distribution of reaction-plane orientations [38,39,42-45] causing non-isotropic azimuthal correlation functions.

For semiclassical reaction models, the impact-parameter averaged correlation function, consistent with Eq. (3), can be written in the form:

$$C(\vec{P},\vec{q}) = N(\vec{P}) \frac{\int bdbd\phi\{\Pi(b,\phi,\frac{1}{2}\vec{P}+\vec{q})\Pi(b,\phi,\frac{1}{2}\vec{P}-\vec{q})C^f(b,\phi,\vec{P},\vec{q})\}}{\int bdbd\phi\{\Pi(b,\phi,\frac{1}{2}\vec{P}+\vec{q})\}\int bdbd\phi\{\Pi(b,\phi,\frac{1}{2}\vec{P}-\vec{q})\}} \quad . \tag{A1}$$

Here, b denotes the impact parameter; ϕ denotes the azimuthal orientation of the reaction plane; $\Pi(b,\phi,\vec{p})$ is the probability of emitting a particle with momentum $\vec{p}$ for events characterized by b and ϕ; $C^f(b,\phi,\vec{P},\vec{q})$ is the correlation function due to final state interactions and/or quantum statistics for given b and ϕ; $N(\vec{P})$ is a suitably chosen normalization constant which makes the normalization at large relative momenta consistent with the experimental data. We can write this expression in the form:

$$C(\vec{P},\vec{q}) = N(\vec{P})\cdot C^f(\vec{P},\vec{q})\cdot C^d(\vec{P},\vec{q}) \left\{ \frac{\int bdbd\phi\{\Pi(b,\phi,\frac{1}{2}\vec{P}+\vec{q})\Pi(b,\phi,\frac{1}{2}\vec{P}-\vec{q})C^f(b,\phi,\vec{P},\vec{q})\}}{\int bdbd\phi\{\Pi(b,\phi,\frac{1}{2}\vec{P})\Pi(b,\phi,\frac{1}{2}\vec{P})C^f(b,\phi,\vec{P},\vec{q})\}} \right.$$

$$\left. \times \frac{\int bdbd\phi\{\Pi(b,\phi,\frac{1}{2}\vec{P})\Pi(b,\phi,\frac{1}{2}\vec{P})\}}{\int bdbd\phi\{\Pi(b,\phi,\frac{1}{2}\vec{P}+\vec{q})\Pi(b,\phi,\frac{1}{2}\vec{P}-\vec{q})\}} \right\} , \tag{A2}$$

with

$$C^f(\vec{P},\vec{q}) = \frac{\int bdbd\Phi\{\Pi(b,\Phi,\frac{1}{2}\vec{P})\Pi(b,\Phi,\frac{1}{2}\vec{P})C^f(b,\Phi,\vec{P},\vec{q})\}}{\int bdbd\Phi\{\Pi(b,\Phi,\frac{1}{2}\vec{P})\Pi(b,\Phi,\frac{1}{2}\vec{P})\}} , \qquad (A3)$$

$$C^d(\vec{P},\vec{q}) = \frac{\int bdbd\Phi\{\Pi(b,\Phi,\frac{1}{2}\vec{P}+\vec{q})\Pi(b,\Phi,\frac{1}{2}\vec{P}-\vec{q})\}}{\int bdbd\Phi\{\Pi(b,\Phi,\frac{1}{2}\vec{P}+\vec{q})\}\int bdbd\Phi\{\Pi(b,\Phi,\frac{1}{2}\vec{P}-\vec{q})\}} . \qquad (A4)$$

Here, $C^f(\vec{P},\vec{q})$ is the correlation function due to final state interactions and/or quantum statistics, renormalized to unity for large relative momenta for which $C^f(b,\Phi,\vec{P},\vec{q}) = 1$, and $C^d(\vec{P},\vec{q})$ is the "dynamical correlation function" which describes correlations caused by averaging over b and Φ.

In Eq. (A2), the terms in curly brackets can be neglected to a good approximation. [If the correlation function $C^f(b,\Phi,\vec{P},\vec{q})$ is independent of b and Φ, the terms in the curly brackets cancel exactly.] For two-proton correlation functions, the correlation function $C^f(b,\Phi,\vec{P},\vec{q})$ is non-trivial only for small relative momenta, $q \lesssim 30$ MeV/c, for which one may approximate $\Pi^2(b,\Phi,\frac{1}{2}\vec{P}) \approx \Pi(b,\Phi,\frac{1}{2}\vec{P}+\vec{q})\Pi(b,\Phi,\frac{1}{2}\vec{P}-\vec{q})$. This approximation reduces the two factors in the curly brackets to unity. At larger relative momenta, $C^f(b,\Phi,\vec{P},\vec{q}) \approx 1$ and the denominators and enumerators of the two terms in the curly brackets cancel cross-wise. It should, therefore, be reasonable to use the approximation:

$$C(\vec{P},\vec{q}) = N(\vec{P})\cdot C^f(\vec{P},\vec{q})\cdot C^d(\vec{P},\vec{q}) . \qquad (A5)$$

With Eq. (A5), one can incorporate dynamical correlations in a fairly straightforward fashion. (Note, however, that other physical processes, not considered in our calculations, may also affect the correlations at small total momenta, e.g. distortions in the Coulomb field of the heavy reaction residue or feeding from the decay of particle unbound states.)

In our measurements, distortions due to dynamical correlations may be present in some of the correlation functions extracted for low total

momenta. For example, there is evidence for shape distortions in the correlation function for the $^{14}N+^{197}Au$ reaction at small total momenta, see Fig. 7. More significant are the difficulties encountered in the normalization of transverse and longitudinal correlation functions for the ^{14}N-induced reactions at low total momenta, see Figs. 16 and 17. However, the present BUU calculations do not provide an accurate description of the cross sections for such low-energy emissions, see Fig. 13. Furthermore, dynamical correlations test different aspects of the model than correlations due to final state interactions. Therefore, we have decided to neglect them in our calculations and used Eq. (A3) for the calculation of the impact parameter averaged correlation functions. For comparisons with experimental data, the calculated correlation functions were renormalized at larger relative momenta, $q \gtrsim 60$ MeV/c, to make them consistent with the normalization conventions adopted in our data analysis.

References

1. For a recent review, see e.g. D.H. Boal, C.K. Gelbke, and B.K. Jennings, Rev. Mod. Phys. 62, 553 (1990).
2. S.E. Koonin, Phys. Lett. 70B, 43 (1977).
3. F. Zarbakhsh, A.L. Sagle, F. Brochard, T.A. Mulera, V. Perez-Mendez, R. Talaga, I. Tanihata, J.B. Carroll, K.S. Ganezer, G. Igo, J. Oostens, D. Woodard, and R. Sutter, Phys. Rev. Lett. 46, 1268 (1981).
4. W.G. Lynch, C.B. Chitwood, M.B. Tsang, D.J. Fields, D.R. Klesch, C.K. Gelbke, G.R. Young, T.C. Awes, R.L. Ferguson, F.E. Obenshain, F. Plasil, R.L. Robinson and A.D. Panagiotou, Phys. Rev. Lett. 51, 1850 (1983).
5. H.A. Gustafsson, H.H. Gutbrod, B. Kolb, H. Löhner, B. Ludewigt, A.M. Poskanzer, T. Renner, H. Riedesel, H.G. Ritter, A. Warwick, F. Weik, and H. Wieman, Phys. Rev. Lett. 53, 544 (1984).
6. Z. Chen, C.K. Gelbke, J. Pochodzalla, C.B. Chitwood, D.J. Fields, W.G. Lynch and M.B. Tsang, Phys. Lett. B186, 280 (1987).
7. Z. Chen, C.K. Gelbke, W.G. Gong, Y.D. Kim, W.G. Lynch, M.R. Maier, J. Pochodzalla, M.B. Tsang, F. Saint-Laurent, D. Ardouin, H. Delagrange, H. Doubre, J. Kasagi, A. Kyanowski, A. Péghaire, J. Péter, E. Rosato, G. Bizard, F. Lefèbvres, B. Tamain, J. Québert, and Y.P. Viyogi, Phys. Rev. C36, 2297 (1987).
8. J. Pochodzalla, C.K. Gelbke, W.G. Lynch, M. Maier, D. Ardouin, H. Delagrange, H. Doubre, C. Grégoire, A. Kyanowski, W. Mittig, A. Péghaire, J. Péter, F. Saint-Laurent, B. Zwieglinski, G. Bizard, F. Lefèbvres, B. Tamain, and J. Québert, Y.P. Viyogi, W.A. Friedman, and D.H. Boal, Phys. Rev. C35, 1695 (1987).
9. J. Pochodzalla, C.B. Chitwood, D.J. Fields, C.K. Gelbke, W.G. Lynch, M.B. Tsang, D.H. Boal, and J.C. Shillcock, Phys. Lett. B174, 36 (1986).
10. S. Pratt and M.B. Tsang, Phys. Rev. C36, 2390 (1987).
11. D. Fox, D.A. Cebra, J. Karn, C. Parks, A. Pradhan, A. Vander Molen, J. van der Plicht, G.D. Westfall, W.K. Wilson, and R.S. Tickle, Phys. Rev. C38, 146 (1988).

12. T.C. Awes, R.L. Ferguson, F.E. Obenshain, F. Plasil, G.R. Young, S. Pratt, Z. Chen, C.K. Gelbke, W.G. Lynch, J. Pochodzalla, and H.M. Xu, Phys. Rev. Lett. 61, 2665 (1988).
13. P.A. DeYoung, M.S. Gordon, Xiu qin Lu, R.L. McGrath, J.M. Alexander, D.M. de Castro Rizzo, and L.C. Vaz, Phys. Rev. C39, 128 (1989).
14. D.A. Cebra, W. Benenson, Y. Chen, E. Kashy, A. Pradhan, A. Vander Molen, G.D. Westfall, W.K. Wilson, D.J. Morrissey, R.S. Tickle, R. Korteling, and R.L. Helmer, Phys. Lett. B227, 336 (1989).
15. J. Québert, R. Boisgard, P. Lautridou, D. Ardouin, D. Durand, D. Goujdami, F. Guilbault, C. Lebrun, R. Tamisier, A. Péghaire, and F. Saint-Laurent, Proceedings of the Symposium on Nuclear Dynamics and Nuclear Disassembly, held at Dallas, April 1989, edited by J.B. Natowitz, World Scientific, Singapore 1989, p. 337.
16. D. Ardouin, F. Guilbault, C. Lebrun, D. Ardouin, S. Pratt, P. Lautridou, R. Boisgard, J. Québert, and A. Péghaire, University of Nantes, Internal Report LPN-89-02.
17. P.A. DeYoung, C.J. Gelderloos, D. Kortering, J. Sarafa, K. Zienert, M.S. Gordon, B.J. Fineman, G.P. Gilfoyle, X. Lu, R.L. McGrath, D.M. de Castro Rizzo, J.M. Alexander, G. Auger, S. Kox, L.C. Vaz, C. Beck, D.J. Henderson, D.G. Kovar, and M.F. Vineyard, Phys. Rev. C41, R1885 (1990).
18. W.G. Gong, C.K. Gelbke, N. Carlin, R.T. de Souza, Y.D. Kim, W.G. Lynch, T. Murakami, G. Poggi, D. Sanderson, M.B. Tsang, H.M. Xu, D.E. Fields, K. Kwiatkowski, R. Planeta, V.E. Viola, Jr., S.J. Yennello, and S. Pratt, Phys. Lett. B246, 21 (1990).
19. W.G. Gong, W. Bauer, C.K. Gelbke, N. Carlin, R.T. de Souza, Y.D. Kim, W.G. Lynch, T. Murakami, G. Poggi, D.P. Sanderson, M.B. Tsang, H.M. Xu, S. Pratt, D.E. Fields, K. Kwiatkowski, R. Planeta, V.E. Viola, Jr., and S.J. Yennello, Phys. Rev. Lett. (to be published).
20. W.G. Gong, W. Bauer, C.K. Gelbke, and S. Pratt, Phys. Rev. C (submitted).
21. W.A. Friedman and W.G. Lynch, Phys. Rev. C28, 16 (1983).
22. J. Aichelin and G. Bertsch, Phys. Rev. C31, 1730 (1985).
23. W. Cassing, Z. Phys. A329, 471 (1988).
24. G.F. Bertsch, Nucl. Phys. A498, 173c (1989).

25. W.G. Gong, Y.D. Kim, G. Poggi, Z. Chen, C.K. Gelbke, W.G. Lynch, M.R. Maier, T. Murakami, M.B. Tsang, H.M. Xu, and K. Kwiatkowski, Nucl. Instr. and Meth. A268, 190 (1988).
26. W.G. Gong, N. Carlin, C.K. Gelbke, and R. Dayton, Nucl. Instr. and Meth. A287, 639 (1990).
27. D.J. Fields, W.G. Lynch, T.K. Nayak, M.B. Tsang, C.B. Chitwood, C.K. Gelbke, R. Morse, J. Wilczynski, T.C. Awes, R.L. Ferguson, F. Plasil, F.E. Obenshain, and G.R. Young, Phys. Rev. C34, 536 (1986).
28. C.K. Gelbke and D.H. Boal, Prog. Part. Nucl. Phys. 19, 33 (1987).
29. B.A. Brown, C.R. Bronk, and P.E. Hodgson, J. Phys. G10, 1683 (1984).
30. R. Wada, D. Fabris, K. Hagel, G. Nebbia, Y. Lou, M. Gonin, J.B. Natowitz, R. Billerey, B. Cheynis, A. Demeyer, D. Drain, D. Guinet, C. Pastor, L. Vagneron, K. Zaid, J. Alarja, A. Giorni, D. Heuer, C. Morand, B. Viano, C. Mazur, C. Ngô, S. Leray, R. Lucas, M. Ribrag, and E. Tomasi, Phys. Rev. C39, 497 (1989).
31. D.X. Jiang, H. Doubre, J. Galin, D. Guerreau, E. Piasecki, J. Pouthas, A. Sokolov, B. Cramer, G. Ingold, U. Jahnke, E. Schwinn, J.L. Charvet, F. Frehaut, B. Lott, C. Magnago, M. Morjean, Y. Patin, Y. Pranal, J.L. Uzureau, B. Gatty, and D. Jacquet, Nucl. Phys. A503, 560 (1989).
32. H.M. Xu, W.G. Lynch, C.K. Gelbke, M.B. Tsang, D.J. Fields, M.R. Maier, D.J. Morrissey, T.K. Nayak, J. Pochodzalla, D.G. Sarantites, L.G. Sobotka, M.L. Halbert, and D.C. Hensley, Phys. Rev. C40, 186 (1989).
33. G.F. Bertsch, H. Kruse, and S. Das Gupta, Phys. Rev. C29, 673 (1984).
34. G.F. Bertsch and S. Das Gupta, Phys. Rep. 160, 189 (1988).
35. A detailed account of the numerical details is given in W. Bauer, Michigan State University report MSUCL-699, submitted to Phys. Rev. C.
36. J. Knoll, Nucl. Phys. A343, 511 (1980).
37. W.G. Lynch, L.W. Richardson, M.B. Tsang, R.E. Ellis, C.K. Gelbke, and R.E. Warner, Phys. Lett. 108B, 274 (1982).
38. M.B. Tsang, W.G. Lynch, C.B. Chitwood, D.J. Fields, D.R. Klesch, C.K. Gelbke, G.R. Young, T.C. Awes, R.L. Ferguson, F. E. Obenshain, F. Plasil, and R.L. Robinson, Phys. Lett. 148B, 265 (1984).
39. C.B. Chitwood, D.J. Fields, C.K. Gelbke, D.R. Klesch, W.G. Lynch, M.B. Tsang, T.C. Awes, R.L. Ferguson, F.E. Obenshain, F. Plasil, R.L. Robinson, and G.R. Young, Phys. Rev. C34, 858 (1986).

40. W. Bauer, Nucl. Phys. A471, 604 (1987).

41. W. Bauer, G.D. Westfall, D. Fox, and D. Cebra, Phys. Rev. C37, 664 (1988).

42. M.B. Tsang, C.B. Chitwood, D.J. Fields, C.K. Gelbke, D.R. Klesch, W.G. Lynch, K. Kwiatkowski and V.E. Viola, Jr., Phys. Rev. Lett. 52, 1967 (1984).

43. M.B. Tsang, Y.D. Kim, N. Carlin, Z. Chen, C.K. Gelbke, W.G. Gong, W.G. Lynch, T. Murakami, T. Nayak, R.M. Ronningen, H.M. Xu, F. Zhu, L.G. Sobotka, D.W. Stracener, D.G. Sarantites, Z. Majka, and V. Abenante, Phys. Rev. C42, R15 (1990).

44. W.K. Wilson, W. Benenson, D.A. Cebra, J. Clayton, S. Howden, J. Karn, T. Li, C.A. Ogilvie, A. Vander Molen, G.D. Westfall, J.S. Winfield, B. Young, and A. Nadasen, Phys. Rev. C41, R1881 (1990).

45. D. Ardouin, Z. Basrak, P. Schuck, A. Péghaire, F. Saint-Laurent, H. Delagrange, H. Doubre, C. Grégoire, A. Kyanowski, W. Mittig, J. Péter, Y.P. Viyogi, J. Québert, C.K. Gelbke, W.G. Lynch, M. Maier, J. Pochodzalla, G. Bizard, F. Lefèbvres, B. Tamain, B. Remaud, and F. Sébille, Nucl. Phys. A514, 564 (1990).

Table 1: Fit parameters used for the description of the inclusive single proton cross sections shown in Fig. 3. The spectra for the ^{14}N and ^{129}Xe-induced reactions were fit with Eq. (1) and (2), respectively. The normalization constants N_i are given in units of [mb/(sr·MeV$^{3/2}$)]. Also given are the velocities, β_{pro} and β_{CN}, of the projectile and the compound nucleus.

Reaction	β_{pro}	β_{CN}	U_c(MeV)	Δ_c(MeV)	i	N_i	β_i	T_i(MeV)
$^{14}N+^{27}Al$	0.40	0.14	1.72	-	1	4.67	0.371	6.04
				-	2	1.62	0.200	19.59
				-	3	3.98	0.073	4.62
$^{14}N+^{197}Au$	0.40	0.026	8.57	-	1	8.52	0.376	5.88
				-	2	4.55	0.200	18.10
				-	3	22.81	0.025	3.84
$^{129}Xe+^{27}Al$	0.26	0.21	5.18	2.0	1	52.40	0.234	4.07
					2	3.91	0.213	8.94
$^{129}Xe+^{27}Al$	0.26	0.21	7.25	2.0	1	36.57	0.213	6.0
$^{129}Xe+^{122}Sn$	0.26	0.13	4.23	2.0	1	66.05	0.241	4.25
					2	7.13	0.130	13.92
$^{129}Xe+^{122}Sn$	0.26	0.13	9.88	2.0	1	58.0	0.130	9.13

Figure Captions:

Fig. 1. Illustration of source functions for emission from short-lived (upper part) and long-lived (lower part) nuclear systems. The dots indicate the locations of protons of a given momentum after the last proton has been emitted.

Fig. 2. Polar coordinates of detector geometry used in this experiment.

Fig. 3. Inclusive proton cross sections measured, at Θ_{lab}=18° and 33°, for the reactions $^{129}Xe+^{27}Al$ and $^{129}Xe+^{122}Sn$ at E/A=31 MeV (left hand panels) and the reactions $^{14}N+^{27}Al$ and $^{14}N+^{197}Au$ at E/A=75 MeV (right hand panels).

Fig. 4. Comparison of energy integrated two-proton correlation functions measured for the reactions $^{14}N+^{27}Al$ and $^{14}N+^{197}Au$ at E/A=75 MeV (top panels) and the reactions $^{129}Xe+^{27}Al$ and $^{129}Xe+^{122}Sn$ at E/A=31 MeV (bottom panels). The solid curves represent correlation functions predicted for Gaussian sources of negligible lifetime for the indicated radius parameters, r_0.

Fig. 5. Two-proton correlation functions measured for the reactions $^{129}Xe+^{27}Al$ and $^{129}Xe+^{122}Sn$ at E/A=31 MeV. The gates on the total momenta, P, of the coincident proton pairs are indicated; solid and open points represent center-of-mass energies below and above the compound nucleus Coulomb barriers.

Fig. 6. Two-proton correlation functions measured for the reaction $^{14}N+^{27}Al$ at E/A=75 MeV. The gates placed on the total momenta, P, of the coincident particle pairs are indicated. The solid curves represent calculations for Gaussian sources of negligible lifetime assuming a dependence of the radius parameter, r_0, on total momentum, P, as shown by the open points in Fig. 8 and folded with the response of the experimental apparatus.

Fig. 7. Two-proton correlation functions measured for the reaction $^{14}N+^{197}Au$ at E/A=75 MeV. The gates placed on the total momenta, P, of the

coincident particle pair are indicated. The solid curves represent calculations for Gaussian sources of negligible lifetime assuming a dependence of the radius parameter, r_0, on total momentum as shown by the solid points in Fig. 8 and folded with the response of the experimental apparatus.

Fig. 8. Radius parameters, r_0, for Gaussian sources of negligible lifetime extracted from two-proton correlation functions gated by different total momenta, P, of the coincident particle pairs for ^{14}N induced reactions on ^{27}Al and ^{197}Au at E/A=75 MeV. The error bars indicate estimated systematic errors.

Fig. 9. Monte-Carlo simulation for the response of the experimental apparatus. The curves show the undistorted correlation functions assumed for the indicated gates on total momentum, P. The points represent the calculated response of the apparatus after taking the energy and angular resolution effects into account. The error bars show the statistical accuracy of the Monte-Carlo calculations.

Fig.10. Two-proton correlation functions measured for the $^{129}Xe+^{27}Al$ (part a) and $^{129}Xe+^{122}Sn$ (parts b,c) reactions at E/A=31 MeV for the indicated gates on the total momenta, P, of the two-proton pairs. The curves represent calculations for evaporative sources at rest in the center-of-mass frame of reference; the parameters are indicated on the figure.

Fig.11. Two-proton correlation functions measured for the $^{129}Xe+^{27}Al$ (part a) and $^{129}Xe+^{122}Sn$ (part b) reactions at E/A=31 MeV for the indicated gates on the total momenta, P, of the two-proton pairs. The curves represent calculations for evaporative sources at rest in the projectile frame of reference; the parameters are indicated on the figure.

Fig.12. Longitudinal (Ψ=0°-40° or Ψ=140°-180°) and transverse (Ψ=60°-120°) two-proton correlation functions measured for the reaction $^{129}Xe+^{27}Al$ (top panel) and $^{129}Xe+^{122}Sn$ (bottom panel) at E/A=31 MeV.

Fig.13. Single proton cross sections calculated with the BUU theory (open points) are compared to experimental cross sections (solid points) for the reactions $^{14}N+^{27}Al$ (top panel) and $^{14}N+^{197}Au$ (bottom panel) at E/A=75 MeV. Circular and diamond shaped symbols indicate laboratory angles of 18° and 33°, respectively.

Fig.14. Two-proton correlation functions, measured for the reaction $^{14}N+^{27}Al$ at E/A=75 MeV, are compared with correlation functions predicted with the BUU theory. The gates placed on the total momenta, P, of the coincident particle pair are indicated.

Fig.15. Two-proton correlation functions, measured for the reaction $^{14}N+^{197}Au$ at E/A=75 MeV, are compared with correlation functions predicted with the BUU theory. The gates placed on the total momenta, P, of the coincident particle pair are indicated.

Fig.16. Longitudinal (Ψ=0°-40° or Ψ=140°-180°) and transverse (Ψ=60°-120°) two-proton correlation functions measured for the $^{14}N+^{27}Al$ reaction at E/A=75 MeV. In the left hand panels, longitudinal and transverse correlation functions were normalized independently; in the right hand panels, the normalizations were determined from the Ψ-integrated data.

Fig.17. Longitudinal (Ψ=0°-40° or Ψ=140°-180°) and transverse (Ψ=60°-120°) two-proton correlation functions measured for the $^{14}N+^{197}Au$ reaction at E/A=75 MeV. In the left hand panels, longitudinal and transverse correlation functions were normalized independently; in the right hand panels, the normalizations were determined from the Ψ-integrated data.

Fig.18. Longitudinal (Ψ=0°-40° or Ψ=140°-180°) and transverse (Ψ=60°-120°) two-proton correlation functions predicted by BUU calculations. The left and right hand panels show calculations for the reactions $^{14}N+^{27}Al$ and $^{14}N+^{197}Au$, respectively. The momentum cuts are indicated in the individual panels.

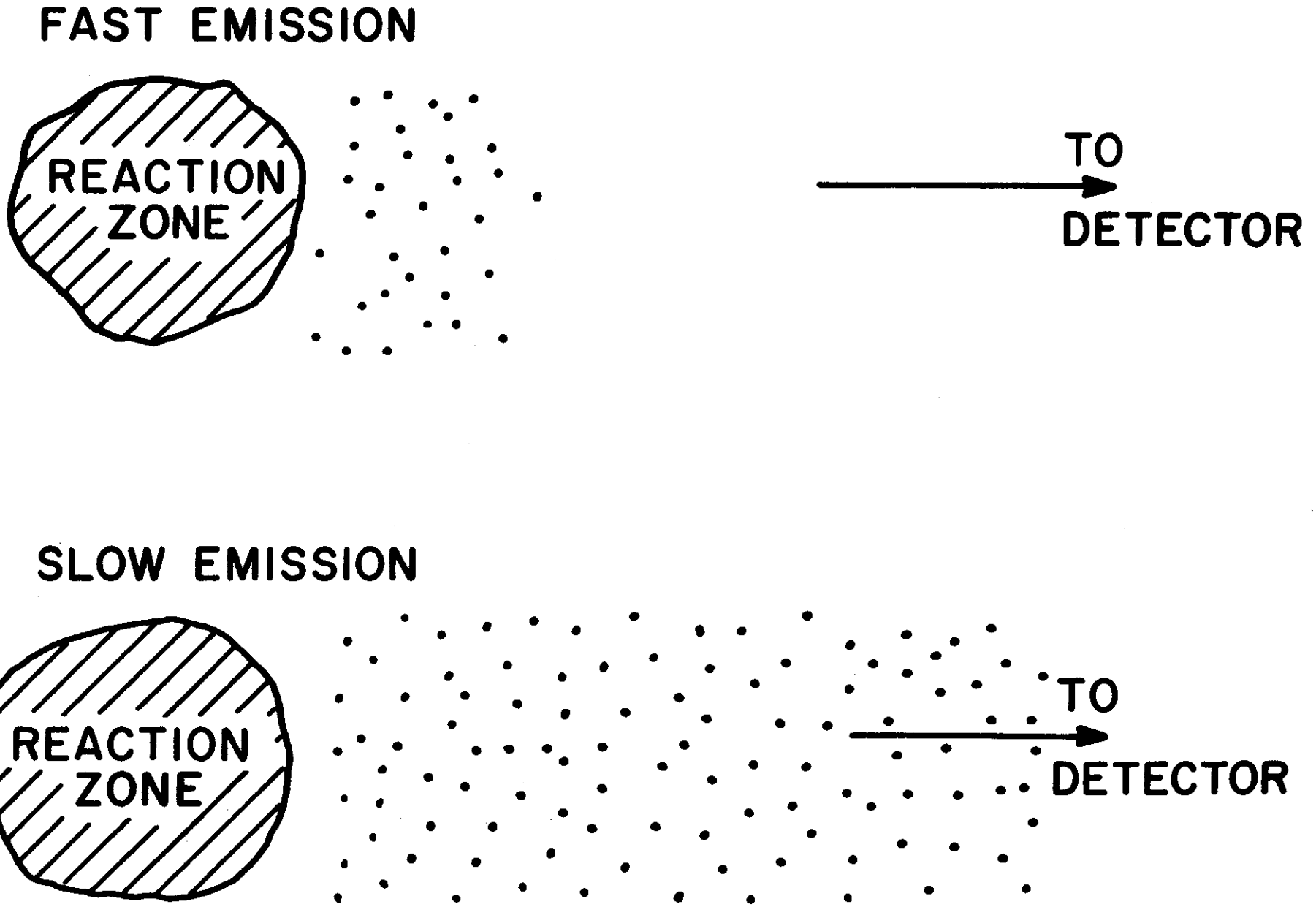
FAST EMISSION
REACTION ZONE
TO DETECTOR
SLOW EMISSION
REACTION ZONE
TO DETECTOR

Fig. 1.6

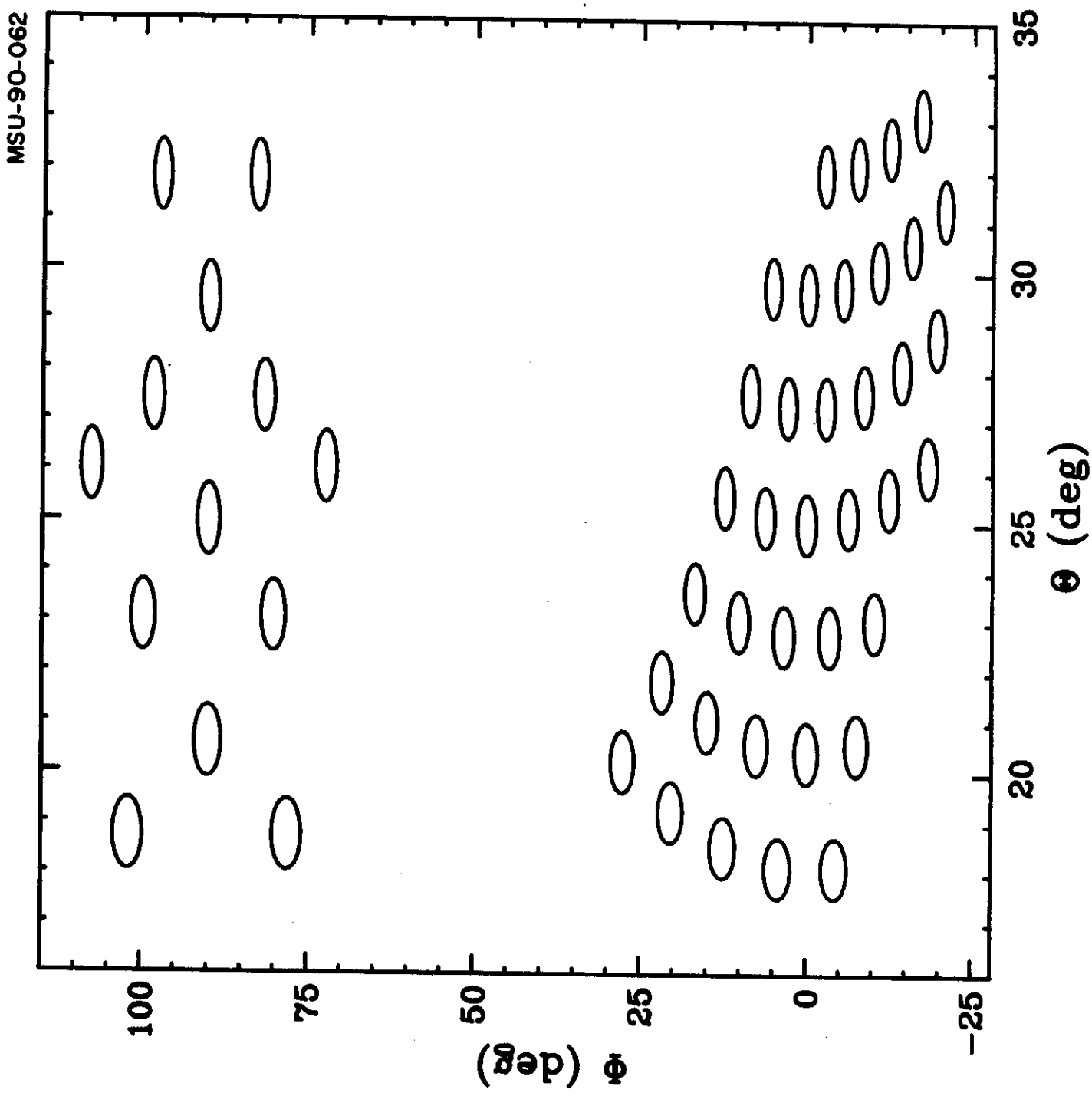

Fig. 2

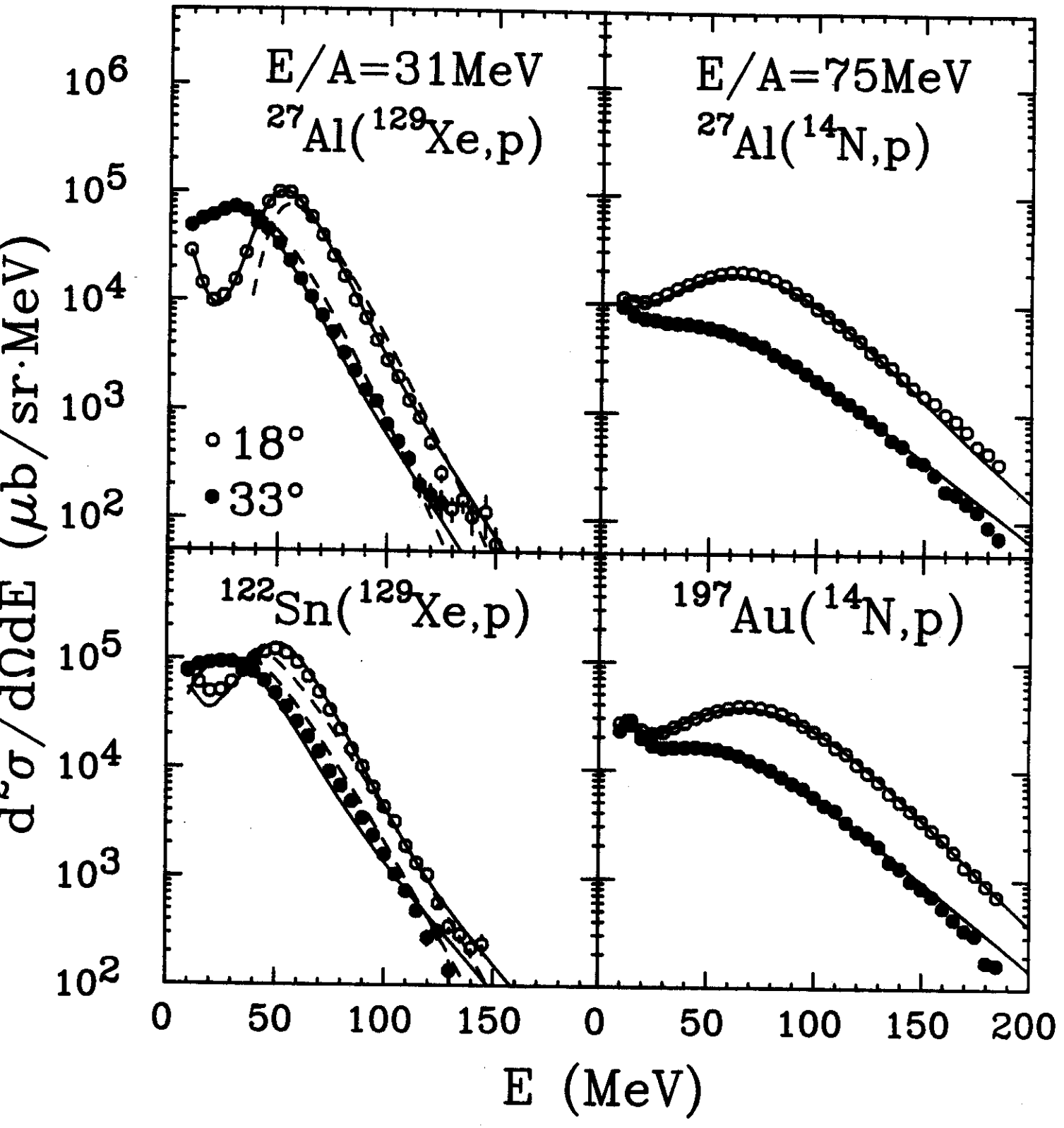
E/A=31MeV
^{27}Al(^{129}Xe,p)
E/A=75MeV
^{27}Al(^{14}N,p)
^{122}Sn(^{129}Xe,p)
^{197}Au(^{14}N,p)
○ 18°
● 33°
$d^2\sigma/d\Omega dE$ (μb/sr·MeV)
10^6
10^5
10^4
10^3
10^2
0
50
100
150
200
E (MeV)

Fig. 3

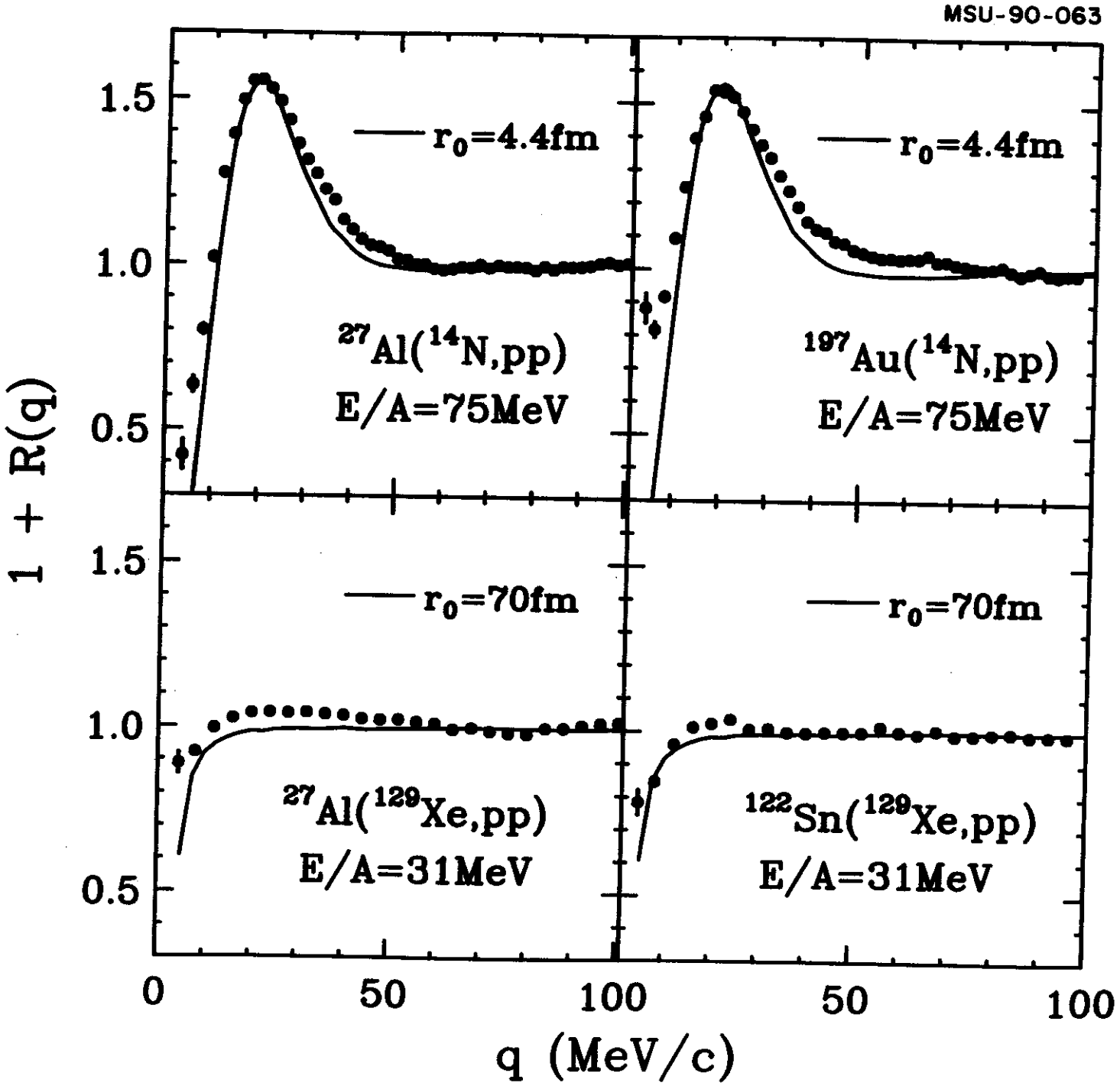
MSU-90-063
1.5
1.0
0.5
1 + R(q)
r_0=4.4fm
^{27}Al(^{14}N,pp)
E/A=75MeV
r_0=4.4fm
^{197}Au(^{14}N,pp)
E/A=75MeV
r_0=70fm
^{27}Al(^{129}Xe,pp)
E/A=31MeV
r_0=70fm
^{122}Sn(^{129}Xe,pp)
E/A=31MeV
0
50
100
50
100
q (MeV/c)

Fig. 4

MSU-90-074

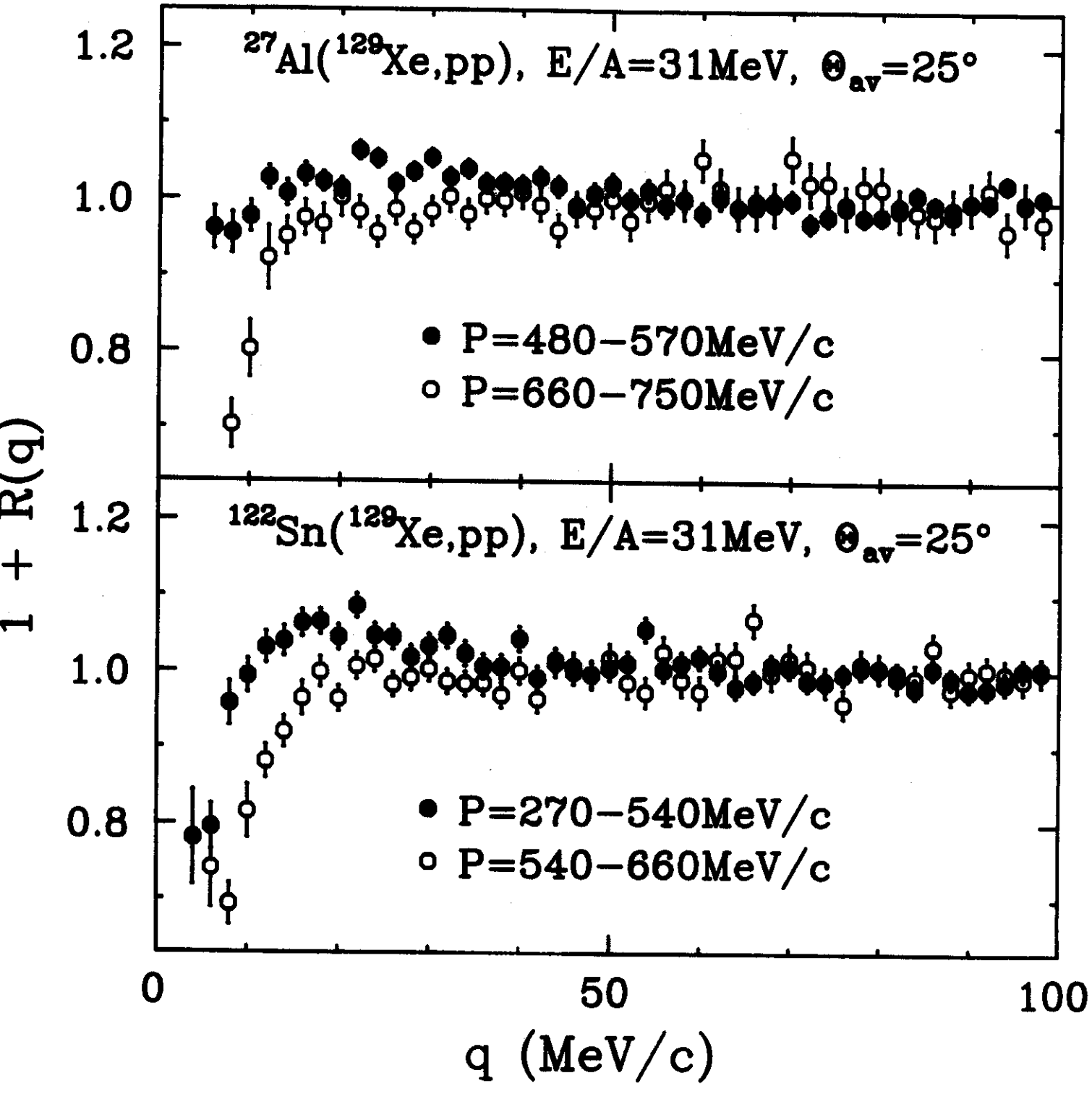

Fig. 5

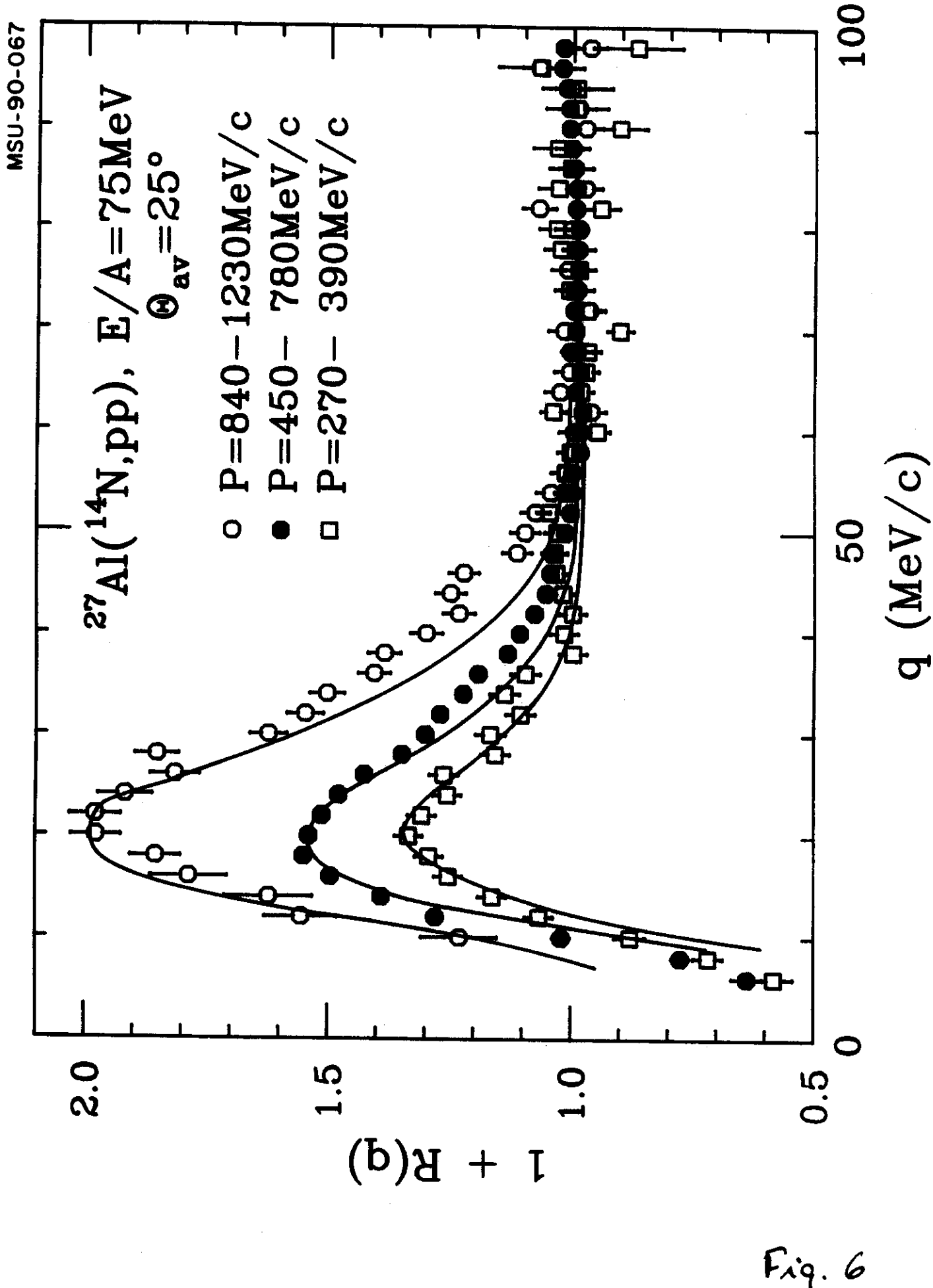
MSU-90-067
^{27}Al(^{14}N,pp), E/A=75MeV
Θ_{av}=25°
P=840−1230MeV/c
P=450− 780MeV/c
P=270− 390MeV/c
1 + R(q)
2.0
1.5
1.0
0.5
0
50
100
q (MeV/c)

Fig. 6

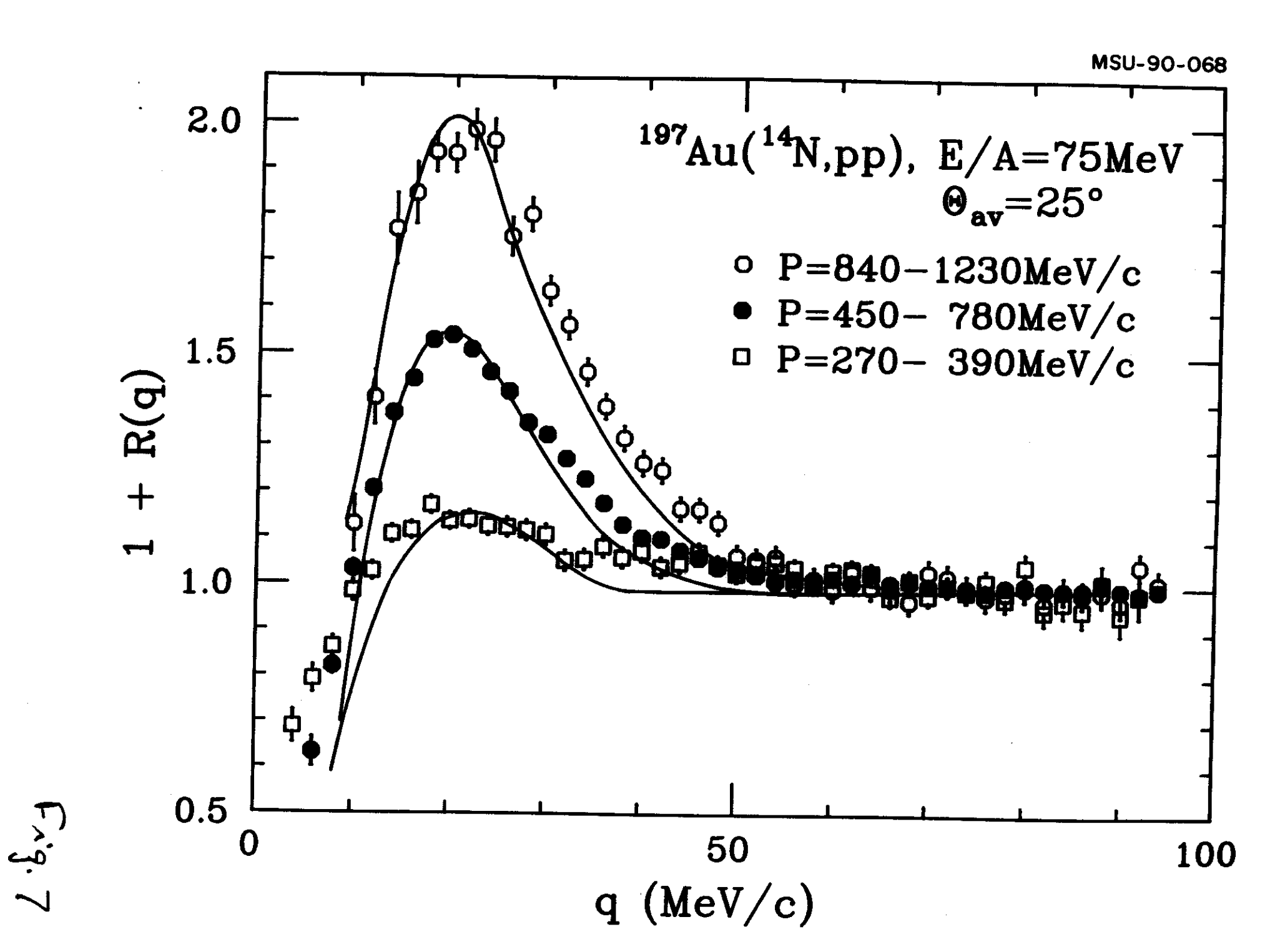
MSU-90-068
^{197}Au(^{14}N,pp), E/A=75MeV
Θ_{av}=25°
P=840−1230MeV/c
P=450− 780MeV/c
P=270− 390MeV/c
1 + R(q)
2.0
1.5
1.0
0.5
0
50
100
q (MeV/c)

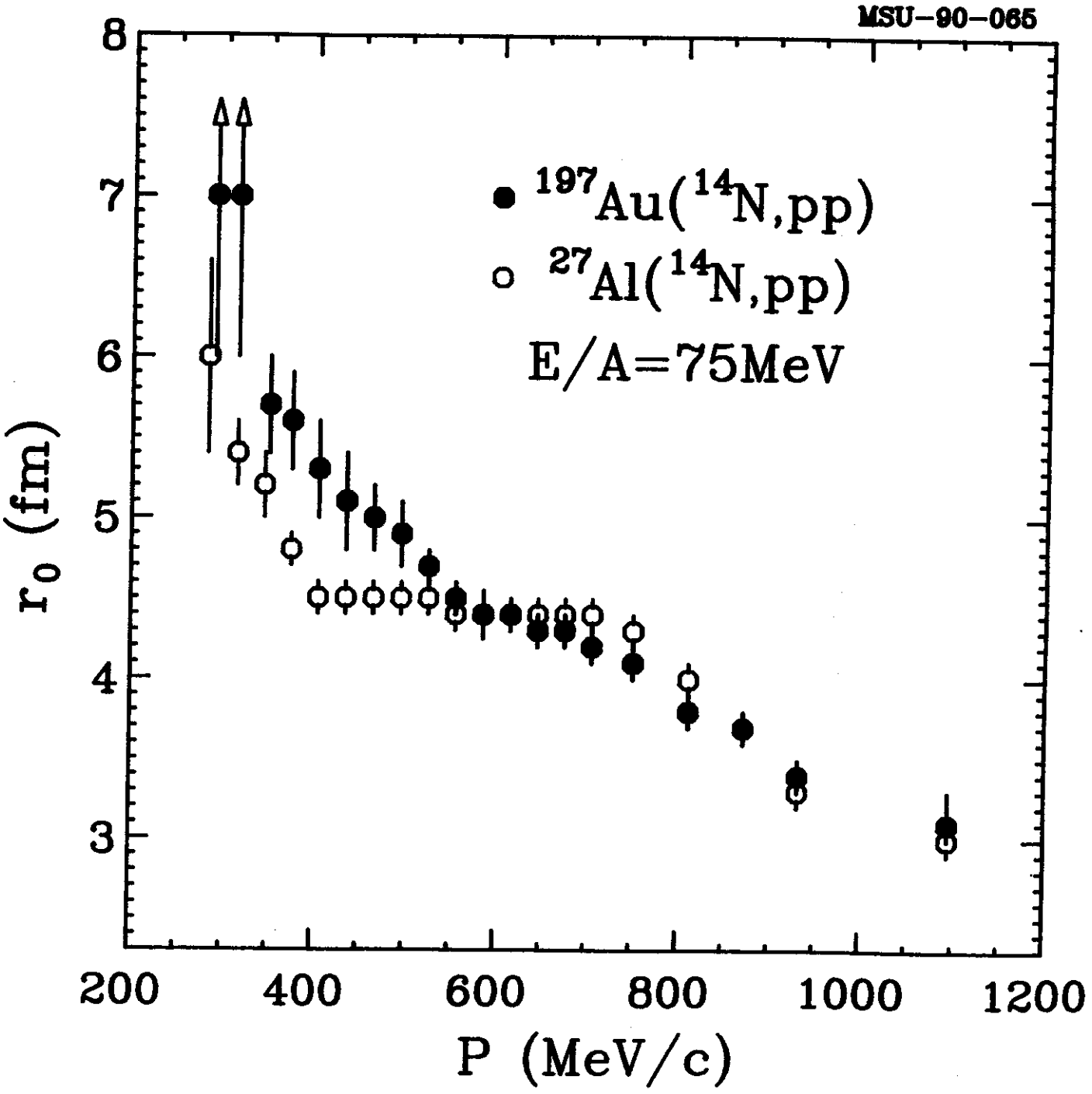
MSU-90-065
^{197}Au(^{14}N,pp)
^{27}Al(^{14}N,pp)
E/A=75MeV
r_0 (fm)
P (MeV/c)
8
7
6
5
4
3
200
400
600
800
1000
1200

Fig. 8

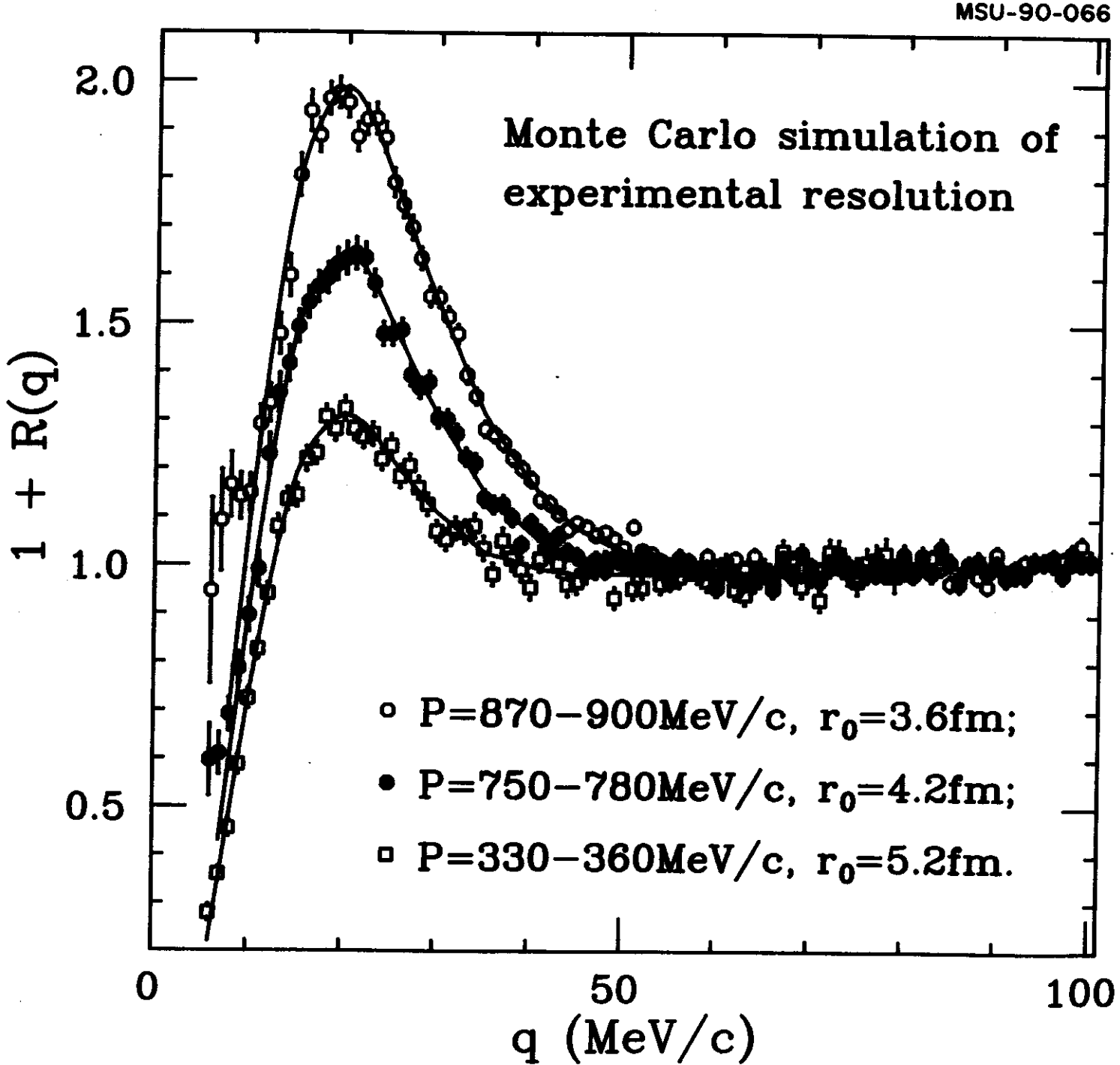
MSU-90-066
Monte Carlo simulation of
experimental resolution
P=870−900MeV/c, r0=3.6fm;
P=750−780MeV/c, r0=4.2fm;
P=330−360MeV/c, r0=5.2fm.
1 + R(q)
q (MeV/c)
2.0
1.5
1.0
0.5
0
50
100

Fig. 9

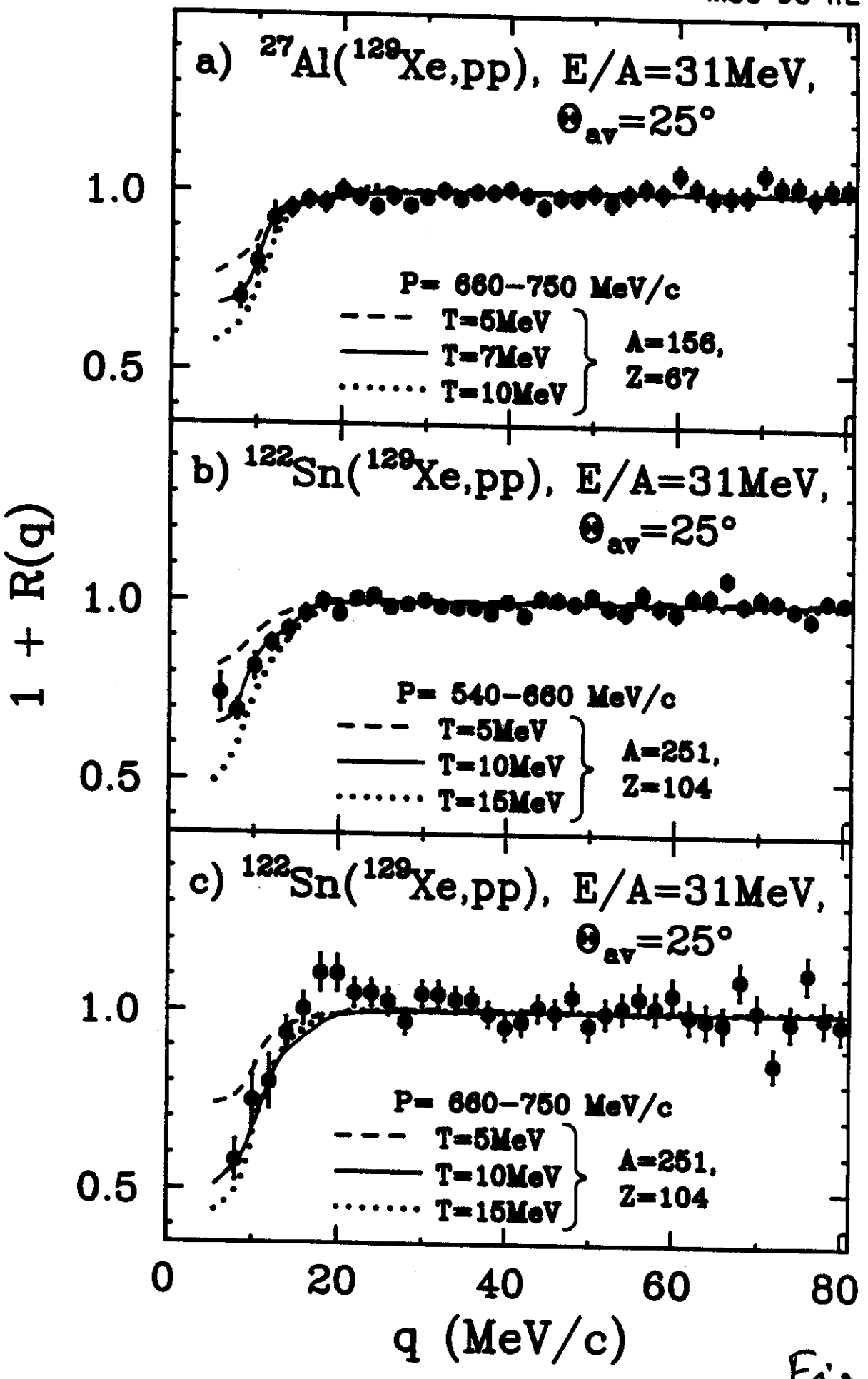
a) ^{27}Al(^{129}Xe,pp), E/A=31MeV,
Θ_{av}=25°
P= 660–750 MeV/c
T=5MeV
T=7MeV
T=10MeV
A=156,
Z=67
b) ^{122}Sn(^{129}Xe,pp), E/A=31MeV,
Θ_{av}=25°
P= 540–660 MeV/c
T=5MeV
T=10MeV
T=15MeV
A=251,
Z=104
c) ^{122}Sn(^{129}Xe,pp), E/A=31MeV,
Θ_{av}=25°
P= 660–750 MeV/c
T=5MeV
T=10MeV
T=15MeV
A=251,
Z=104
1 + R(q)
1.0
0.5
0
20
40
60
80
q (MeV/c)

Fig. 10

MSU-90-194

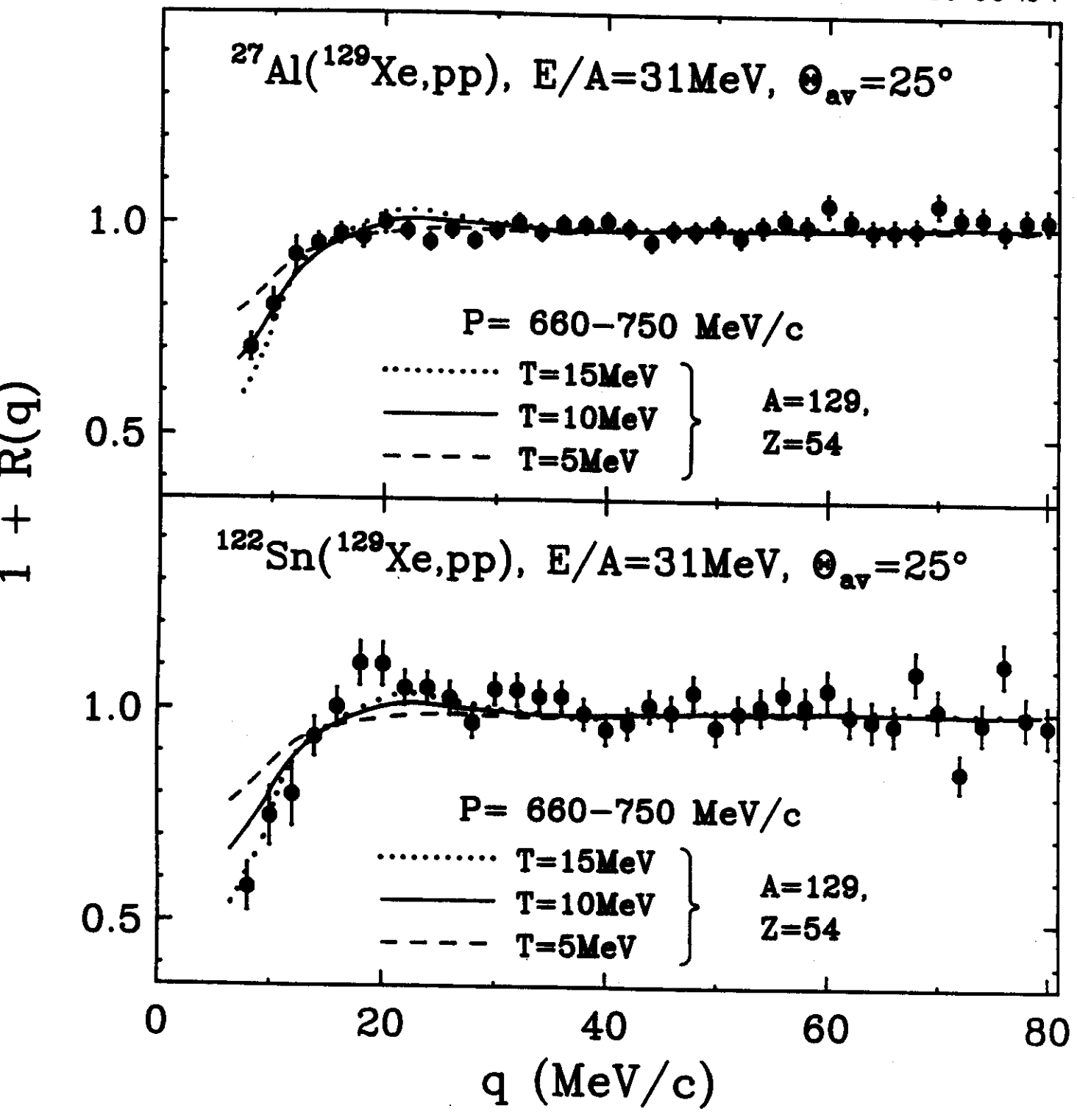

Fig. 11

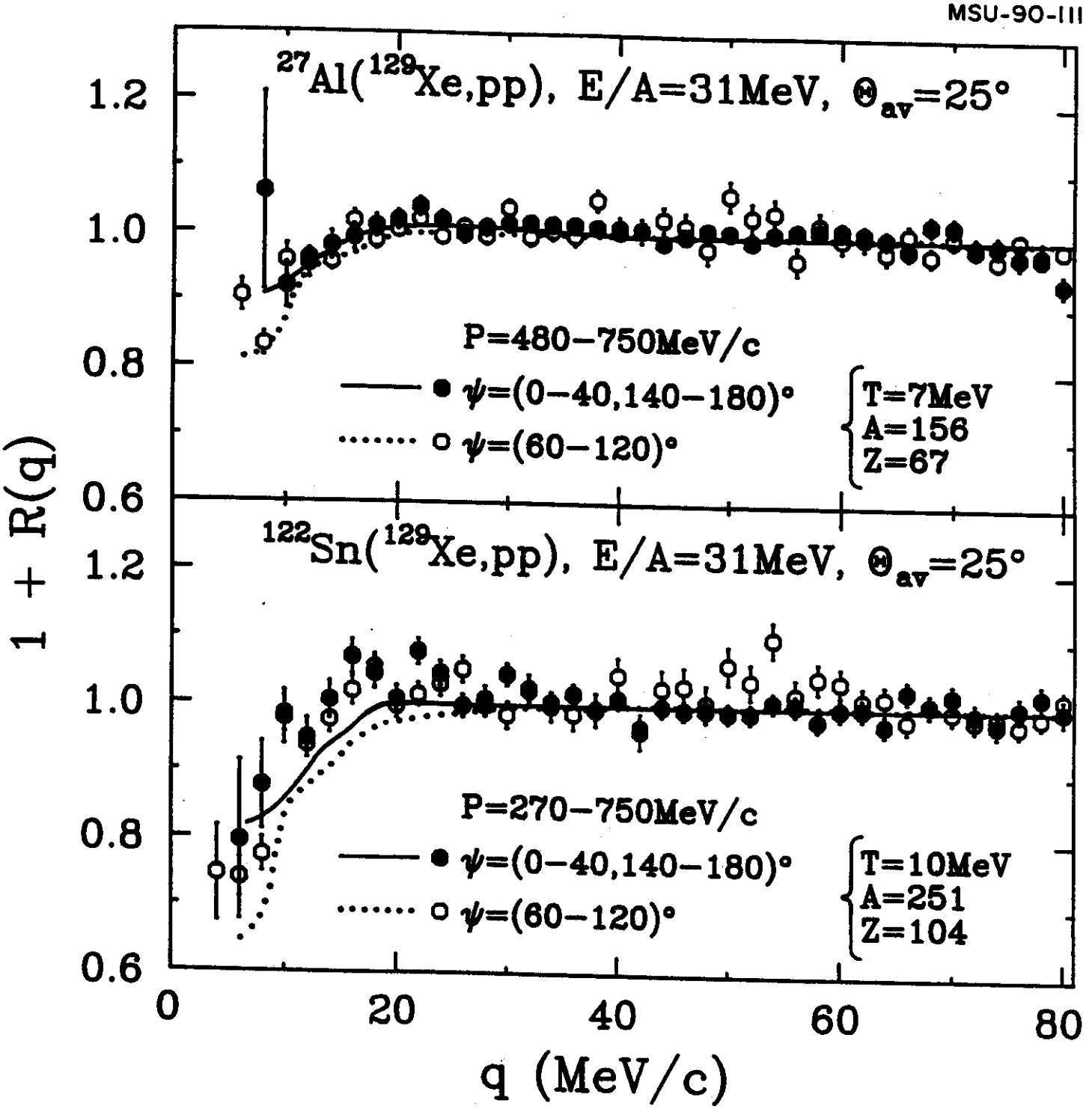
MSU-90-III
^{27}Al(^{129}Xe,pp), E/A=31MeV, Θ_{av}=25°
P=480–750MeV/c
ψ=(0–40,140–180)°
ψ=(60–120)°
T=7MeV
A=156
Z=67
^{122}Sn(^{129}Xe,pp), E/A=31MeV, Θ_{av}=25°
P=270–750MeV/c
ψ=(0–40,140–180)°
ψ=(60–120)°
T=10MeV
A=251
Z=104
1 + R(q)
q (MeV/c)
0.6
0.8
1.0
1.2
0
20
40
60
80

Fig. 12

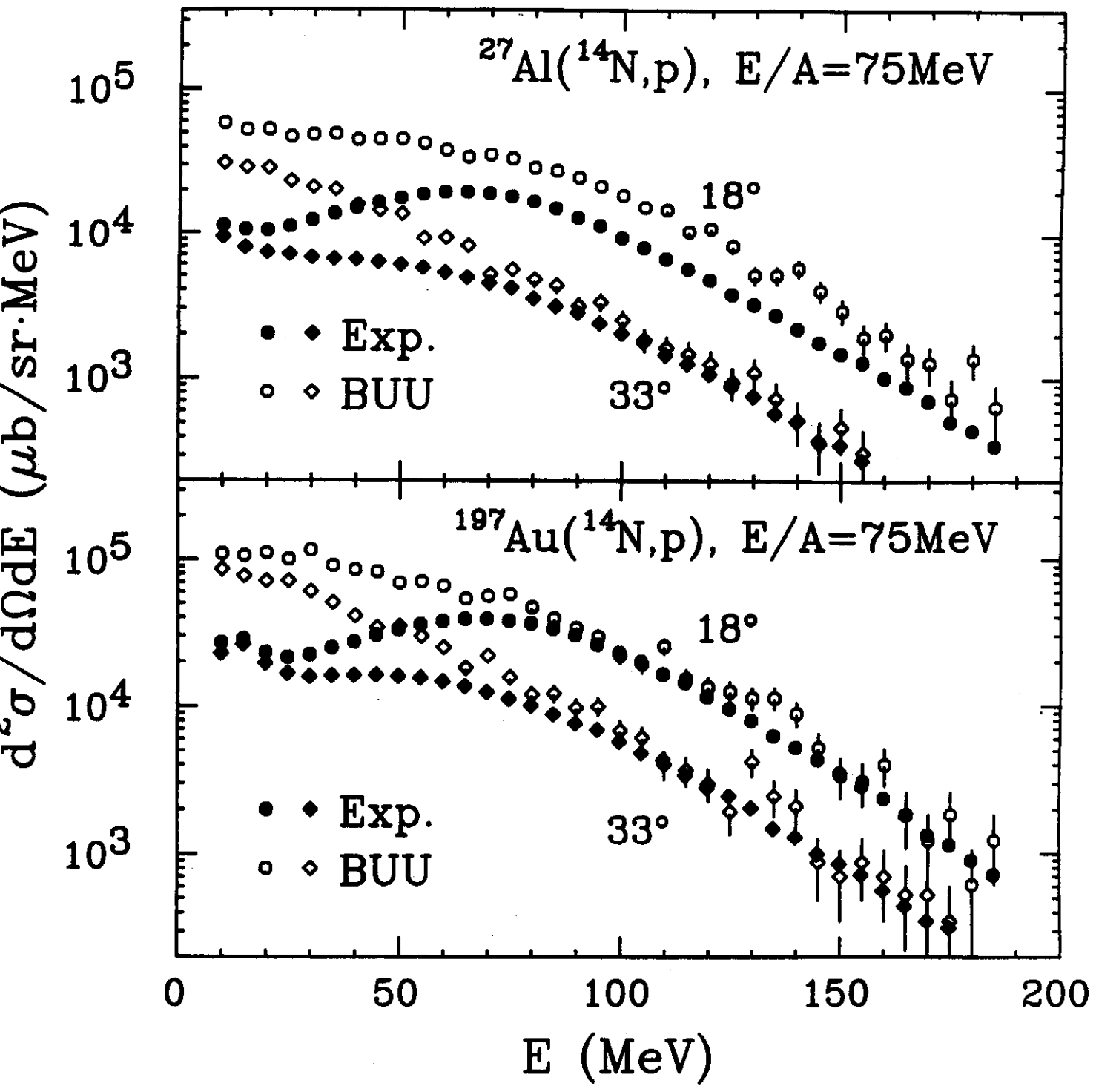
^{27}Al(^{14}N,p), E/A=75MeV
18°
33°
Exp.
BUU
^{197}Au(^{14}N,p), E/A=75MeV
18°
33°
Exp.
BUU
10^5
10^4
10^3
0
50
100
150
200
E (MeV)
$d^2\sigma/d\Omega dE$ (μb/sr·MeV)

Fig. 13

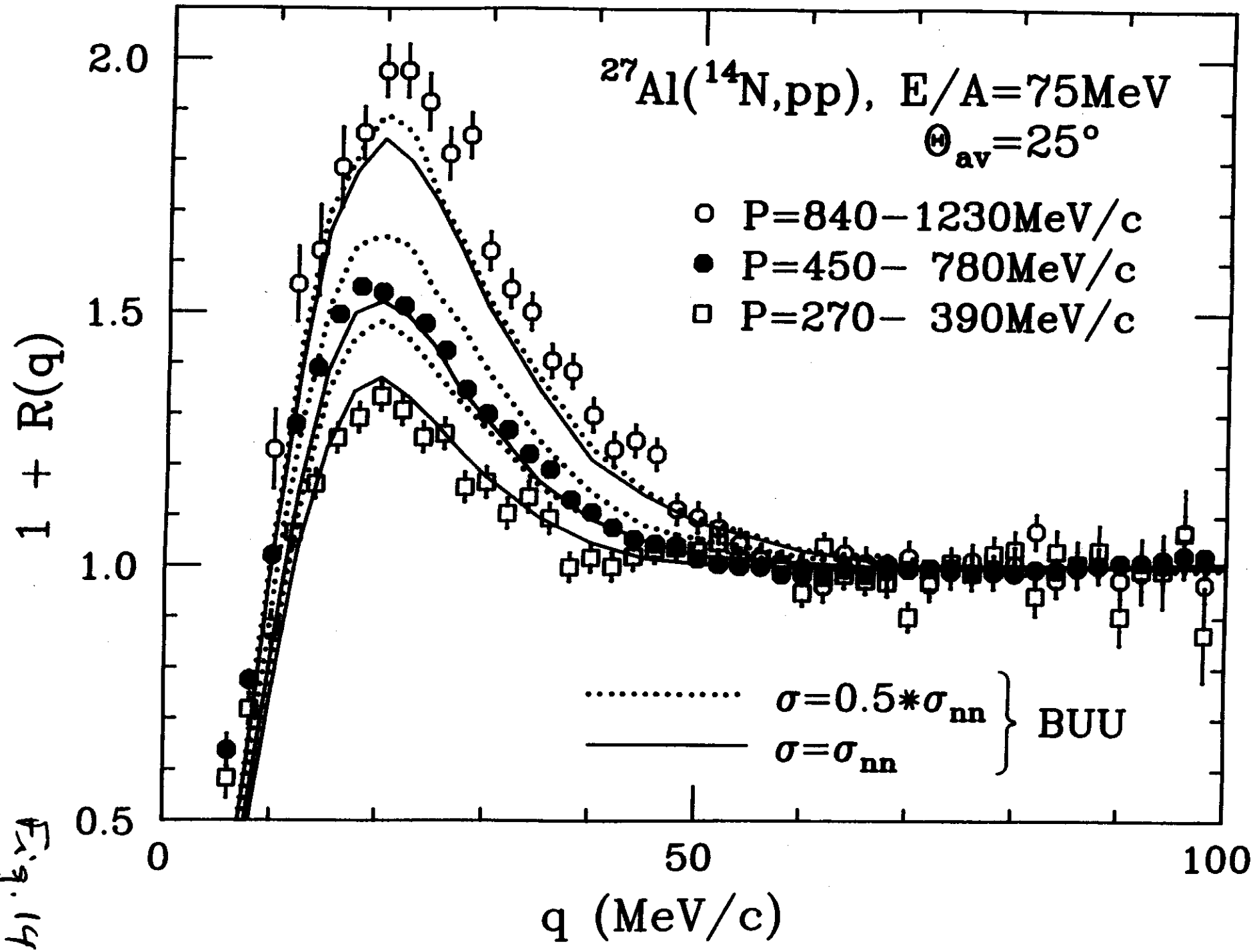
^{27}Al(^{14}N,pp), E/A=75MeV
Θ_{av}=25°
P=840−1230MeV/c
P=450− 780MeV/c
P=270− 390MeV/c
σ=0.5*σ_{nn}
σ=σ_{nn}
BUU
1 + R(q)
q (MeV/c)
2.0
1.5
1.0
0.5
0
50
100

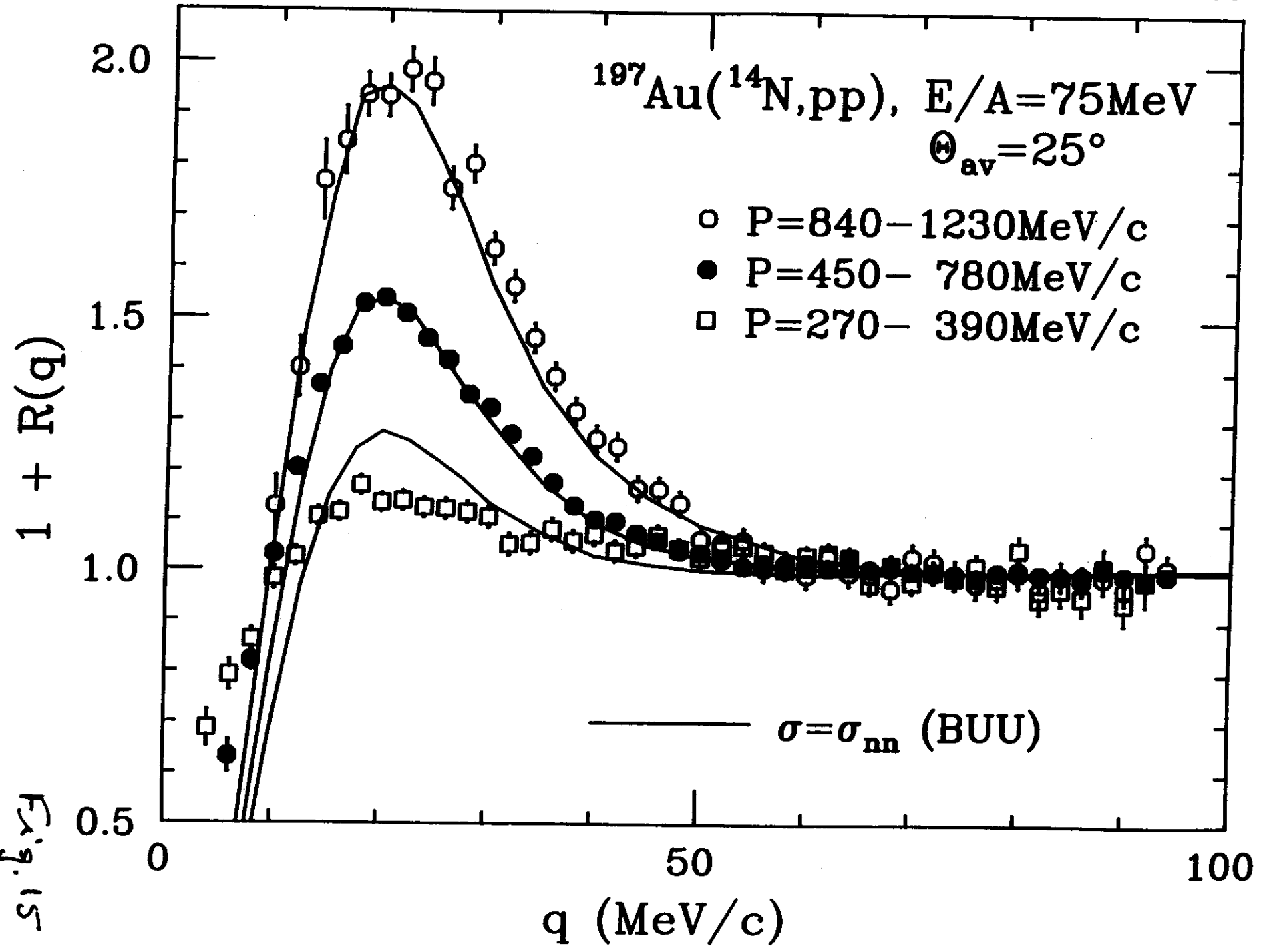
^{197}Au(^{14}N,pp), E/A=75MeV
Θ_{av}=25°
P=840−1230MeV/c
P=450− 780MeV/c
P=270− 390MeV/c
$\sigma=\sigma_{nn}$ (BUU)
1 + R(q)
q (MeV/c)
2.0
1.5
1.0
0.5
0
50
100

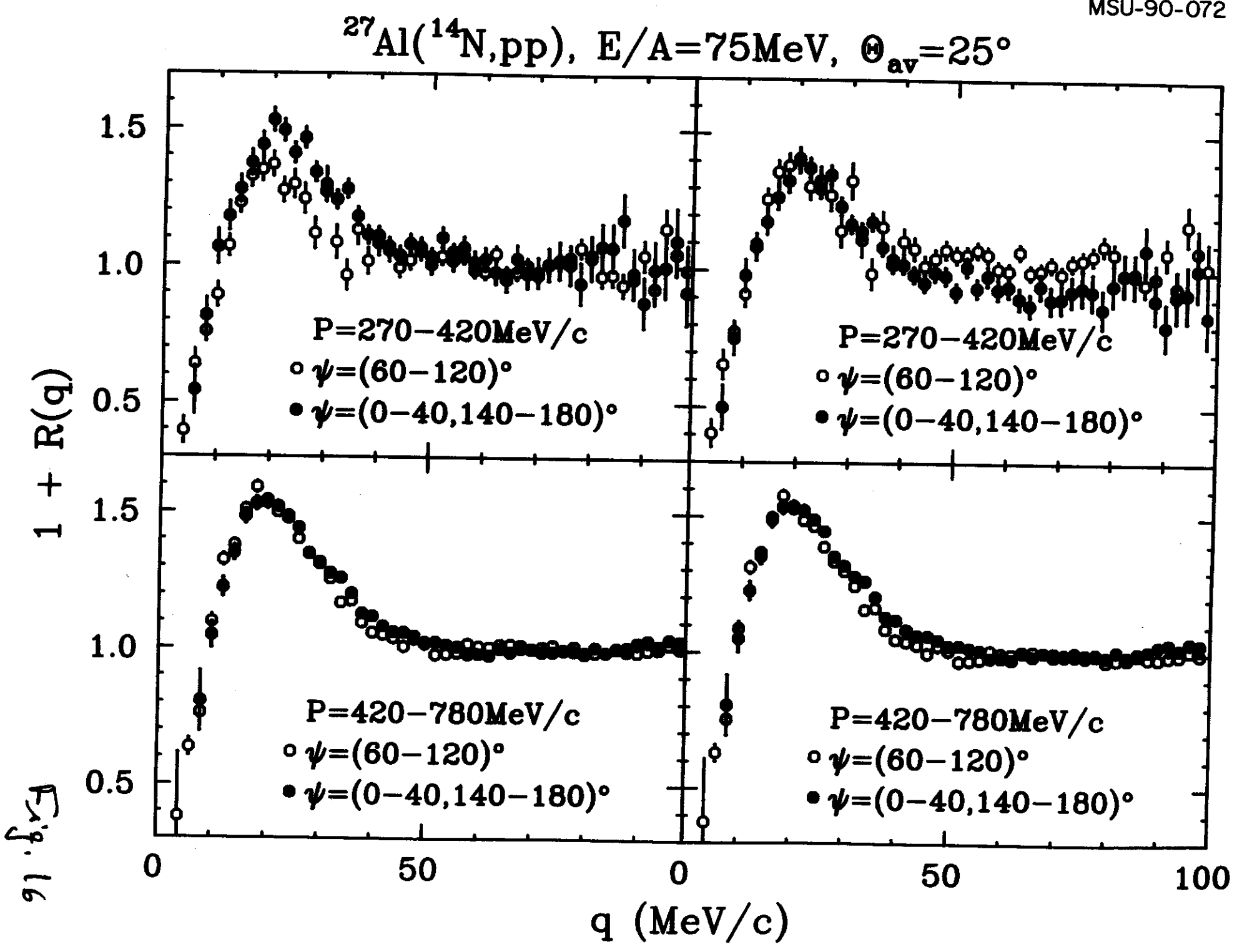
^{27}Al(^{14}N,pp), E/A=75MeV, Θ_{av}=25°
P=270−420MeV/c
ψ=(60−120)°
ψ=(0−40,140−180)°
P=420−780MeV/c
ψ=(60−120)°
ψ=(0−40,140−180)°
1 + R(q)
q (MeV/c)
0
50
100
0.5
1.0
1.5

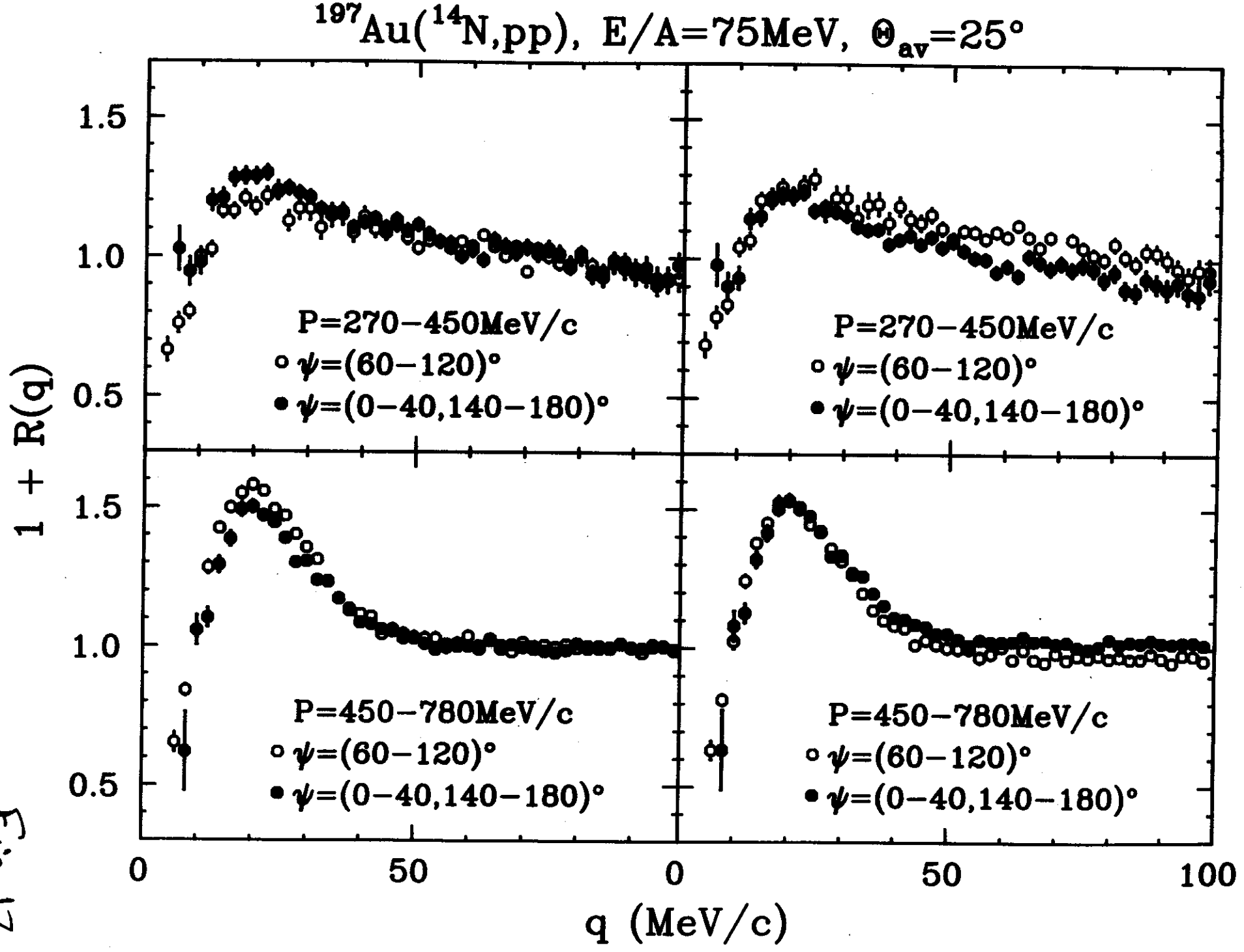
^{197}Au(^{14}N,pp), E/A=75MeV, Θ_{av}=25°
1 + R(q)
q (MeV/c)
P=270−450MeV/c
ψ=(60−120)°
ψ=(0−40,140−180)°
P=450−780MeV/c
ψ=(60−120)°
ψ=(0−40,140−180)°
0.5
1.0
1.5
0
50
100

Fig. 17

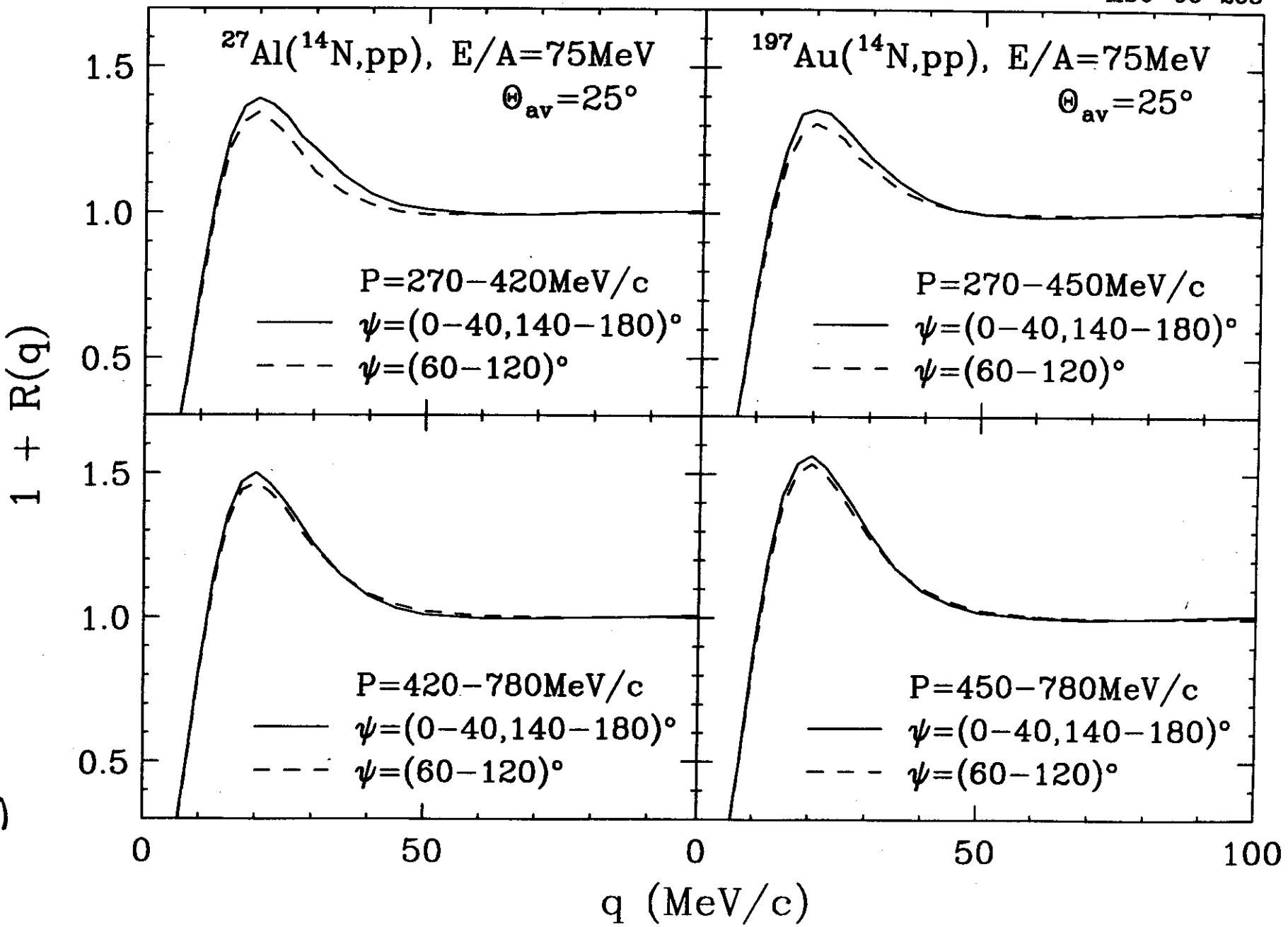
^{27}Al(^{14}N,pp), E/A=75MeV
Θ_{av}=25°
P=270−420MeV/c
ψ=(0−40,140−180)°
ψ=(60−120)°
^{197}Au(^{14}N,pp), E/A=75MeV
Θ_{av}=25°
P=270−450MeV/c
ψ=(0−40,140−180)°
ψ=(60−120)°
P=420−780MeV/c
ψ=(0−40,140−180)°
ψ=(60−120)°
P=450−780MeV/c
ψ=(0−40,140−180)°
ψ=(60−120)°
1 + R(q)
q (MeV/c)
0
50
100
0.5
1.0
1.5

Fig. 18